



# Development of the long-term harmonized multi-satellite SIF (LHSIF) dataset at 0.05° resolution (1995–2024)

Chu Zou<sup>1,2,4</sup>, Shanshan Du<sup>2,4</sup>, Xinjie Liu<sup>2,4</sup>, and Liangyun Liu<sup>2,3,4</sup>

<sup>1</sup>State Key Laboratory of Efficient Utilization of Arable Land in Northern China, National Hulunbeier Grassland Ecosystem Observation and Research Station, Institute of Agricultural Resources and Regional Planning, Chinese Academy of Agricultural Sciences, Beijing 100081, China

<sup>2</sup>Key Laboratory of Digital Earth Science, Aerospace Information Research Institute, Chinese Academy of Sciences, Beijing, 100094, China

<sup>3</sup>University of Chinese Academy of Sciences, Beijing 100049, China

<sup>4</sup>International Research Center of Big Data for Sustainable Development Goals, Beijing 100094, China

**Correspondence:** Liangyun Liu (liuly@radi.ac.cn)

Received: 24 February 2025 – Discussion started: 28 April 2025

Revised: 8 September 2025 – Accepted: 20 September 2025 – Published: 5 January 2026

**Abstract.** Solar-induced chlorophyll fluorescence (SIF) is a crucial proxy of photosynthetic processes in vegetation. In recent decades, advancements in remote sensing technology have facilitated long-term global SIF monitoring, significantly enhancing our understanding of vegetation dynamics on a global scale. Despite this progress, current SIF datasets face major challenges, including temporal inconsistencies among various satellite-derived products and a lack of long-term, high-resolution observations. In this study, we developed a “Long-term Harmonized SIF” (LHSIF) dataset spanning 1995 to 2024 with a fine spatial resolution of 0.05° by coordinating SIF satellite observations from GOME, SCIAMACHY, GOME-2, and OCO-2. Light use efficiency (LUE)-based spatial downscaling models were employed for each SIF product to generate fine-resolution global SIF maps. The long-term dataset was constructed using temporally corrected GOME-2A SIF (TCSIF) as a benchmark and was combined with a cumulative distribution function (CDF) normalization method for far-red SIF harmonization across satellite sensors from GOME, SCIAMACHY, and OCO-2. The resulting harmonized dataset shows a 49 % reduction in inter-sensor differences compared to the uncorrected data and exhibits a stable interannual increase of  $0.31 \pm 0.07 \% \text{ yr}^{-1}$ . This result strongly aligns with the growth rate of gross primary production (GPP,  $0.47 \pm 0.03 \% \text{ yr}^{-1}$ ) and is consistent with ground-based SIF observations ( $R > 0.60$ ). Therefore, the long-term harmonized SIF dataset with a fine 0.05° resolution is valuable for estimating global photosynthesis over extended periods. The LHSIF dataset is available at <https://doi.org/10.5281/zenodo.16394372> (Zou et al., 2025).

## 1 Introduction

Solar-induced chlorophyll fluorescence (SIF) is an optical signal naturally released by plants, closely linked to their photosynthetic dynamics (Zhang et al., 2016; Zhang and Peñuelas, 2023; Zhu et al., 2024; Rascher et al., 2015; Porcar-Castell et al., 2014; Damm et al., 2015; Mohammed et al., 2019). SIF has garnered significant attention due to its potential as a novel proxy for gross primary productivity (GPP) (Ryu et al., 2019), bridging the gap in our understanding of

global photosynthetic processes (Beer et al., 2010; Anav et al., 2015; Chen et al., 2024).

Following the publication of the initial global SIF map from the Greenhouse Gases Observing Satellite (GOSAT), interest in the SIF-GPP association greatly increased (Frankenberg et al., 2011; Guanter et al., 2012; Joiner et al., 2011). Subsequent satellite-based analyses have consistently revealed strong spatial and temporal correlations between SIF and GPP, showcasing remarkable alignment between SIF and GPP in terms of spatial distribution and sea-

sonal variability (Anav et al., 2015; Li et al., 2018; Verma et al., 2017; Yang et al., 2015; Guanter et al., 2014; Zheng et al., 2024). However, these results are mostly based on coarse-resolution SIF datasets such as the Global Ozone Monitoring Experiment (GOME)-2, leading to potential spatial mismatch issues. Additionally, the SIF-GPP link varies by vegetation type, emphasizing the critical need for SIF datasets with higher spatial resolution and spatiotemporal consistency to better support ecosystem monitoring and interpretation.

Long-term global SIF observations are important for analyzing the vegetation functions and changes under different climatic conditions. Multiple high-spectral-resolution satellite missions have provided publicly available global SIF products since 1995. The earliest records originated from the GOME sensor on European Remote sensing Satellite (ERS) in 1995, followed by the SCanning Imaging Absorption spectroMeter for Atmospheric CartographHY (SCIAMACHY) onboard Environmental Satellite (EnviSat) in 2003. However, these sensors had relatively short operational lifespans, ceasing operations in 2003 and 2012, respectively. The GOME-2 sensor onboard the MetOp-A satellite, launched in January 2007, operated until November 2021; this sensor provided the longest SIF time series to date (Joiner et al., 2013). The Orbiting Carbon Observatory (OCO)-2 satellite, launched in 2014, features exceptionally high spatial resolution and has been validated through synchronized airborne campaigns (Sun et al., 2017) to ensure the reliability of resulting SIF products. Recent studies highlight the potential of the TROPOMI sensor onboard Sentinel-5P (Koren et al., 2018; Wen et al., 2020), but its SIF products are currently constrained to a relatively short time series (May 2018 to April 2021).

Despite the availability of multiple satellite SIF products, most have a temporal coverage shorter than 10 years, and large discrepancies have been observed between different SIF products (Parazoo et al., 2019). These temporal inconsistencies may stem from differences in retrieval algorithms, absolute radiometric calibration errors, instrumental artifacts, directional effects, and variations in satellite overpass times and footprint sizes (Zhang et al., 2018c; Bacour et al., 2019). To address these challenges, Wen et al. (2020) proposed a harmonization framework that used the cumulative distribution function (CDF) to integrate SIF datasets from SCIAMACHY and GOME-2 during their overlapping period, resulting in a continuous record from 2002 to 2018.

While Wen's framework laid the foundation for cross-sensor harmonization, it did not explicitly address instrument degradation – a key factor that compromises the long-term consistency of single-sensor records. Such degradation, as observed in GOME-2, poses a significant challenge for long-term consistency and introduces uncertainties in trend analyses (Parazoo et al., 2019). For instance, Yang et al. (2018) reported diverging trends between EVI and SIF, attributing the latter's decline to reduced photosynthetic activity. However, Zhang et al. (2018a) argued that this conclusion was

impacted by the deterioration of the GOME-2A instrument. Further research by Koren et al. (2018) showed that the decline in SIF persisted even after correcting for sensor degradation. The SIFTERv2 product (van Schaik et al., 2020) employed in Koren's study was simply corrected using linear models; the reliability of SIFTERv2 decreased significantly after 2016, limiting its application for long-term trend analysis.

To mitigate this limitation, Wang et al. (2022) attempted to create a temporally corrected long-term SIF product (LT\_SIFc\*) by correcting the degradation trends in gridded GOME, SCIAMACHY, and GOME-2 SIF products. However, the method lacks a physically based correction of the actual sensor radiance degradation and instead applies adjustments on the SIF product, which may not accurately reflect the true instrumental change. This is further complicated by the nonlinear characteristics inherent in the SIF retrieval methodology and subsequent processing procedures (e.g., zero-bias correction and quality filtering), which prevent a direct and linear propagation of sensor degradation into the final SIF retrievals. Recently, the temporally corrected GOME-2A SIF dataset (TCSIF) included a calibration of the radiance measurements of GOME-2A using a pseudo-invariant method (Zou et al., 2024). This correction effectively eliminates the influence of sensor degradation over time, providing a practical reference for generating long-term harmonized SIF products.

So far, the cross-sensor consistency of existing long-term SIF records remains to be further evaluated. In this study, we employed the TCSIF dataset as a physically calibrated benchmark to constrain the long-term consistency of GOME, SCIAMACHY, and OCO-2 SIF observations. By harmonizing these multi-sensor datasets against a radiometrically corrected reference, we generated a continuous and temporally consistent SIF product spanning from 1995 to 2024, which is the longest multi-satellite harmonized SIF dataset to date. Additionally, we performed light use efficiency (LUE)-based spatial downscaling on the coarse spatial resolution dataset derived from the satellite SIF products. This downscaling reduced the spatial difference between satellite-derived SIF and ground-based measurements of SIF and GPP, thereby facilitating our understanding of vegetation photosynthesis at the global scale.

## 2 Method and materials

### 2.1 Satellite-based SIF datasets

#### 2.1.1 GOME SIF

GOME, which was launched in 1995 on the ERS-2 satellite of the European Space Agency (ESA), was initially developed to measure the column densities of ozone and nitrogen dioxide (Hahne et al., 1993). GOME's channel 4 operates within a spectral range of 590–790 nm, achieving a spectral

resolution of about 0.5 nm for far-red SIF retrieval. Although GOME is characterized by a relatively low spatial resolution of  $320 \text{ km} \times 40 \text{ km}$ , it provides the earliest available record of SIF data. The GOME SIF product utilized in this research is the daily averaged SIF signal at 740 nm, which is retrieved by data-driven algorithms (Joiner et al., 2019). The dataset spans the period from July 1995 to June 2003.

### 2.1.2 SCIAMACHY SIF

The SCIAMACHY instrument was in operation from 2002 to 2012 onboard ESA's Envisat satellite, overlapping with the timeframe of GOME. The instrument enhanced GOME's capabilities by offering a finer spatial resolution of  $30 \text{ km} \times 60 \text{ km}$ . The comparable spectral ranges and spectral resolutions of SCIAMACHY and GOME allowed for the use of analogous techniques for SIF retrievals. The SCIAMACHY SIF products we used were retrieved using the same data-driven algorithms and fitting window (734–758 nm) as those used for GOME. Daily SCIAMACHY SIF datasets at 740 nm from January 2003 to April 2012 were employed (Joiner et al., 2021).

### 2.1.3 GOME-2A SIF

As a successor to GOME, GOME-2 is part of EUMETSAT's MetOp satellite series, with three satellites (MetOp-A, B, and C) launched between 2007 and 2018. GOME-2 improved upon its predecessor by providing enhanced spatial resolution ( $40 \text{ km} \times 40 \text{ km}$  or  $80 \text{ km} \times 40 \text{ km}$ , contingent upon the specific platform utilized). The GOME-2A SIF datasets were obtained from the MetOp-A satellite, launched in 2007 and operating until 2021.

Research has shown apparent differences between GOME-2A SIF products using different retrieval methods (Parazoo et al., 2019). For instance, SIF retrieval using a fitting window of 720–758 nm and a backward elimination algorithm (Köhler et al., 2015) yields values up to twice as large as the retrievals using a 734–758 nm window (Joiner et al., 2013). The GOME-2A SIF dataset used in this study was retrieved using the same data-driven algorithm and fitting window as Joiner et al. (2013), ensuring consistency with GOME and SCIAMACHY SIF. Furthermore, the GOME-2 SIF we use has undergone correction for sensor degradation and was found to avoid spurious trends caused by instrument deterioration (Zou et al., 2024). Therefore, this temporal-corrected GOME-2A SIF dataset with degradation correction is used as a benchmark to harmonize the data from the other three sensors.

### 2.1.4 OCO-2 SIF

OCO-2 was a satellite mission launched by the National Aeronautics and Space Administration in 2014. Unlike earlier missions, OCO-2 focuses on small target areas, attain-

ing a considerably greater spatial resolution of approximately  $1.3 \text{ km} \times 2.3 \text{ km}$ . The spectral range of OCO-2 extends from 757 to 775 nm, facilitating the initial SIF retrievals at 757 and 771 nm. Drawing upon the empirical correlation of SIF across various wavelengths, the product offers daily global SIF at 740 nm (OCO-2/OCO-3 Science Team et al., 2020). The SIF datasets from OCO-2 and GOME-2 have eight overlapping years (2014 to 2021). As a result, a thorough comparison and validation of the consistency can be conducted between the two datasets.

The product specifications and sensor information are listed in Table 1. This study resampled the orbital SIF data from different satellites into global gridded datasets of varying sizes according to the footprint and the global coverage of the satellites. Satellite-derived SIF measurements from GOME, SCIAMACHY, GOME-2, and OCO-2 were aggregated into monthly maps with grid sizes of  $1^\circ \times 1^\circ$ ,  $1^\circ \times 1^\circ$ ,  $0.5^\circ \times 0.5^\circ$ , and  $1^\circ \times 1^\circ$ , respectively.

## 2.2 Spatial downscaling

An LUE-based model was used for downscaling the gridded SIF datasets with coarse spatial resolutions. Assuming that SIF can be represented using the LUE model in a manner that is comparable to GPP (Berry et al., 2012; Guanter et al., 2014; Damm et al., 2015), then:

$$\text{SIF} = \text{PAR} \times \text{fPAR} \times \text{SIF}_{\text{yield}} \quad (1)$$

where  $\text{SIF}_{\text{yield}}$  is the fluorescence quantum yield, which is influenced by hydric and thermic stresses. fPAR represents the fraction of photosynthetically active radiation (PAR) that is absorbed by vegetation, which exhibits a positive correlation with vegetation indices. Assuming that PAR is uniformly distributed over small areas and can be considered constant, then Eq. (1) can be further expressed as (Duveiller and Cescatti, 2016; Duveiller et al., 2020):

$$\text{SIF} \approx b_0 \times f(\text{NIRv}) \times f(\text{VPD}) \times f(\text{AT}) \quad (2)$$

where NIRv is the near-infrared reflectance of vegetation, VPD represents vapor pressure deficit (accounts for the effect of hydric stresses), and AT is the air temperature at 2 m (accounts for the impact of thermic stresses). A quadratic function, sigmoid function, and Gaussian function with unknown coefficients were used to express  $f(\text{NIRv})$ ,  $f(\text{VPD})$ , and  $f(\text{AT})$ , respectively, as follows:

$$\begin{aligned} \text{SIF} \approx b_1 \text{NIRv}^{b_2} &\times \left[ \frac{1}{(1 + \exp(b_3(b_4 - \text{VPD})))} \right] \\ &\times \left[ \exp \left( -0.5 \left( \frac{\text{AT} + b_5}{b_6} \right)^2 \right) \right]. \end{aligned} \quad (3)$$

The unknown coefficients  $b_1$  to  $b_6$  in Eq. (3) can be determined by a nonlinear iterative approach. Here, we implemented this approach using the "L-BFGS-B" algorithm (Byrd et al., 1995).

**Table 1.** Information on multiple satellite SIF datasets used to construct long-term SIF products.

Satellite/ Sensor	Temporal range	Footprint Size (km <sup>2</sup> )	Equatorial overpass time (Local time)	Swath width (km)	Wavelength (nm)	Grid size	Reference
ERS-2/ GOME	Jul 1995– Jun 2003	40 × 320	10:30	960	740	1° × 1°	Joiner et al. (2019)
Envisat/ SCIAMACHY	Jan 2003– Apr 2012	30 × 240/ 30 × 60	10:00	960/240	740	1° × 1°	Joiner et al. (2021)
MetOp-A/ GOME-2	Jan 2007– Nov 2021	40 × 80/ 40 × 40	09:30	1920/960	740	0.5° × 0.5°	Zou et al. (2024)
OCO-2	Sep 2014– Dec 2024	1.3 × 2.2	13:30	10.3	757/771	1° × 1°	OCO-2/OCO-3 Science Team et al. (2020)

NIRv, VPD, and AT were the three driving variables of the spatial downscaling model. NIRv datasets characterized by a spatial resolution of 0.05° were partially derived from the Advanced Very High Resolution Radiometer (AVHRR) (Jeong et al., 2024) for 1995–2021, while the NIRv for 2022–2024 were calculated using MODIS MCD43C4 nadir reflectance (Schaaf and Wang, 2021). AT and VPD data for 1995–2024 were obtained from the TerraClimate product with an original spatial resolution of 1/24° (Abatzoglou et al., 2018). The driving variables were aggregated to coarse spatial resolutions (0.5° × 0.5° for GOME-2 and 1° × 1° for other satellites) for training the LUE model described in Eq. (3) and to estimate the coefficients ( $b_1$  to  $b_6$ ). The 50 closest neighbors of the center pixel were utilized to train the LUE model in an 11 × 11 sliding window. Subsequently, SIF datasets, characterized by a spatial resolution of 0.05°, were produced by inputting the 0.05° driving variables into the trained model. Since the coefficients ( $b_1$  to  $b_6$ ) were computed for each coarse-resolution pixel, gridded artifacts may appear in the final product. To further ensure smooth spatial transitions, for each high-resolution pixel within a coarse-resolution pixel, a 3 × 3 block of coarse-resolution pixels was selected, and nine sets of six coefficients ( $b_1$  to  $b_6$ ) were computed. Meanwhile, a fine-resolution (0.05°) weighting grid was established within the 3 × 3 low-resolution pixels using a two-dimensional Gaussian function with a standard deviation of 15 km. The final downscaled result for each high-resolution pixel was obtained as the weighted average of the nine sets of model-predicted values, following the approach of Duveiller and Cescatti (2016).

### 2.3 CDF matching method

The cross-sensor SIF normalization was implemented using a stratified CDF matching approach to account for environmental variability. Specifically, the stratification was done based on a combination of Köppen climate zones (Beck et al.,

2023) and the MODIS land cover types product (MCD12C1; Friedl and Sulla-Menashe, 2022). The land cover map of the central year within the overlapping period was used to construct the CDFs, while the CDFs were applied each year according to the yearly land cover types. For the period before 2001, when MCD12C1 data were unavailable, the land cover map of 2001 was applied. The degradation-corrected GOME-2A dataset was used as the normalization reference for all other satellite-derived SIF datasets, based on their overlapping periods. The normalization of GOME data was based on the SCIAMACHY dataset, which had been previously normalized with GOME-2 data.

For each sensor pair, the cumulative distribution functions of both the reference and target datasets were calculated across their overlapping temporal coverage. A linear interpolation was used to match the quantiles of the target dataset with those of the reference. Separate CDF transfer functions were derived for each calendar month to account for phenological variations. For SCIAMACHY and GOME, due to the limited temporal overlap, the entire period (from January to June 2003) was used to construct the CDF function. The complete workflow is shown in Fig. 1.

Further, the discrepancy between the two SIF time series can be quantified by the mean squared difference (MSD):

$$MSD = \frac{1}{n} \sum_{i=1}^n (D_{1i} - D_{2i})^2 \quad (4)$$

where  $D_1$  and  $D_2$  are the SIF time series of the two SIF datasets to be compared.  $i$  represents the  $i$ th month of the chosen period. Furthermore, Eq. (1) can be broken down into three terms (Bacour et al., 2019):

$$MSD = (\overline{D_1} - \overline{D_2})^2 + (\sigma_{D_1} - \sigma_{D_2})^2 + 2\sigma_{D_1}\sigma_{D_2}(1 - r) \quad (5)$$

where  $\overline{D_1}$  and  $\overline{D_2}$  are the expected values of the time series, while  $\sigma_{D_1}$  and  $\sigma_{D_2}$  signify the respective standard deviations. Additionally,  $r$  is the Pearson correlation coefficient

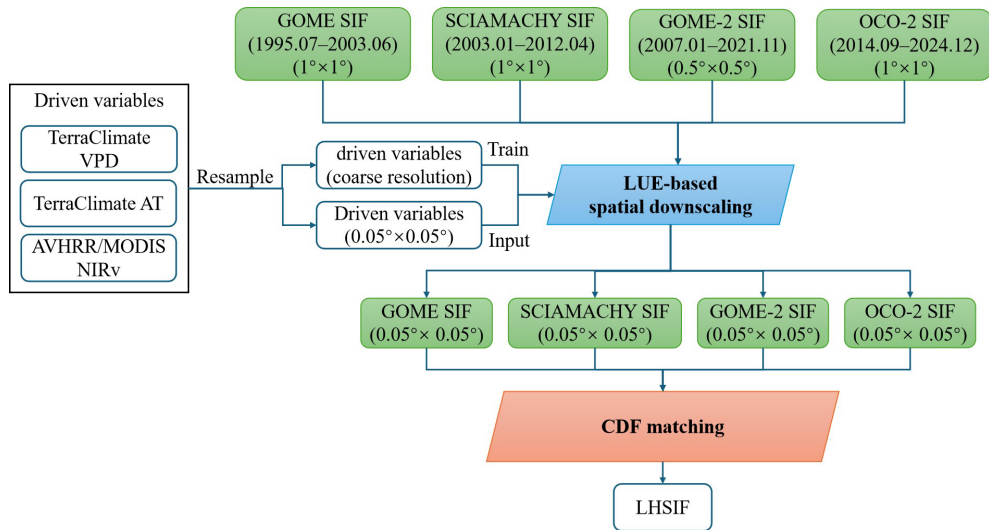


**Figure 1.** The workflow for spatial downscaling and temporal alignment for generating the LHSIF products from 1995 to 2024.

that quantifies the relationship between the datasets. The first and second terms in the formula represent the square of the mean deviation (denoted as bias<sup>2</sup>) and difference in standard deviation (denoted as variance<sup>2</sup>) between the corrected datasets and the target datasets. The final term quantifies the inconsistency of the linear correlation between the two datasets (denoted as phase).

#### 2.4 Temporal Trend Analysis Metrics

To assess long-term trends in vegetation dynamics, we employed the Mann-Kendall (MK) test, a non-parametric method suitable for detecting monotonic trends in time series data, using the Python package `pyMannKendall` (Hussain and Mahmud, 2019). Trend estimation uncertainty was quantified by the standard deviation and 95 % confidence intervals of the estimated temporal trend.

#### 2.5 Datasets for validation and comparison analysis

Multiple long-term satellite-derived products were utilized for cross-validation in this study. Key characteristics of these benchmark datasets, along with the proposed LHSIF product, are summarized in Table 2.

##### 2.5.1 Boreal Ecosystem Productivity Simulator GPP

The Boreal Ecosystem Productivity Simulator (BEPS) is an ecological process model that integrates vegetation parameters with meteorological data to simulate ecosystem productivity. We used the GPP dataset generated by the BEPS model for 1995–2019 (Ju and Zhou, 2021). The original spatial resolution of the dataset is  $0.072727^\circ \times 0.072727^\circ$ , providing fine-scale insights into productivity dynamics. This high-resolution dataset allows for detailed spatiotemporal analysis

and facilitates comparisons with downscaled SIF datasets in this study to help our understanding of ecosystem carbon dynamics.

##### 2.5.2 Long-term satellite SIF products

The LT\_SIFc\* dataset provides long-term SIF retrievals corrected for temporal inconsistencies between GOME, SCIAMACHY, and GOME-2 SIF datasets (Wang et al., 2022). A CDF method was employed for the harmonization of different SIF datasets, and the LUE-based model was used for spatial downscaling. The LT\_SIFc\* dataset spans 1995 to 2018 at a spatial resolution of  $0.05^\circ \times 0.05^\circ$ .

The SIF\_005 dataset is a SIF product spanning 2003 to 2017, with a spatial resolution of  $0.05^\circ \times 0.05^\circ$  (Wen et al., 2020). This product integrates data from SCIAMACHY and GOME-2 SIF datasets, and it is downscaled using a machine learning-based method. The v2.2 (trend\_corrected) version was utilized in this study; the original SIF dataset used for this version has been preliminarily corrected for temporal degradation.

The LCSIF dataset provides global SIF estimates from 1982 to 2022 at  $0.05^\circ \times 0.05^\circ$  resolution, derived from bias-corrected AVHRR and MODIS reflectance data (Fang et al., 2023). A neural network (NN) model was trained to predict OCO-2 SIF using two surface reflectance bands (red and near-infrared), after inter-sensor radiometric calibration between AVHRR and MODIS during their overlapping period.

##### 2.5.3 AVHRR vegetation indices

Global NDVI and NIRv datasets from 1995 to 2021, derived from the AVHRR sensors, were utilized in this study. These datasets were developed by Jeong et al. (2024) based on the AVHRR Long-Term Data Record version 5 (LTDR

**Table 2.** The long-term products used in this study and relevant details about them.

Dataset	Description	Time coverage	Sensors for SIF product	Processing method
LHSIF	Multi-sensor harmonized SIF with extended temporal coverage	Jul 1995–Dec 2024	GOME, SCIAMACHY, GOME-2, OCO-2	CDF matching
LT_SIFc*	Multi-sensor harmonized SIF	Jul 1995–Dec 2018	GOME, SCIAMACHY, GOME-2	CDF matching
SIF_005	Harmonized SIF	Jan 2003–Dec 2017	SCIAMACHY, GOME-2	CDF matching
LCSIF	Spatially continuous reconstructed SIF	Jan 1982–Dec 2023	OCO-2	Neural network
BEPS GPP	Simulated GPP using ecological process model	Jan 1981–Dec 2019	–	–
AVHRR NDVI	Long term NDVI product addressed for temporal inconsistency	Jan 1982–Dec 2021	–	–
AVHRR NIRv	Long term NIRv product addressed for temporal inconsistency	Jan 1982–Dec 2021	–	–

V5) surface reflectance product. To address temporal inconsistency in long-term AVHRR records, a three-step correction was applied, including cross-sensor calibration, orbital drift correction, and machine learning-based harmonization with MODIS vegetation indices. This post-processing significantly improved the temporal consistency of NDVI and NIRv from 1982 to 2021, as verified using detrended anomalies and trends at calibration sites. The final product enables more robust analyses of long-term vegetation dynamics and reduces spurious trends due to sensor artifacts.

#### 2.5.4 Ground-based observations

Ground-based SIF and GPP observations were integrated into this study to validate and enhance the interpretation of satellite-derived datasets. Specifically, FLUXNET GPP observations were employed, which are based on in-situ measurements from a global network of flux towers distributed across diverse ecosystems (Pastorello et al., 2020). FLUXNET sites with more than five years of data were grouped into climate zones and vegetation functional types (see Fig. S1 in the Supplement for site distribution and types). The field “GPP\_DT\_VUT\_REF” was used. To ensure the quality of the GPP data used for validation, only GPP records with the quality flag greater than 0.7 (Verma et al., 2015) were retained in this study.

In addition, tower-based SIF observations from the ChinaSpec network, including sites such as DM, GC, HL, XTS, and AR (Zhang et al., 2021), were used to validate the accuracy and spatiotemporal consistency of the long-term SIF dataset generated in this study. The locations and cover types of the ChinaSpec sites used are listed in Table S1 in the Supplement. To ensure consistent comparisons, the tower-based

SIF at 760.6 nm was converted to 740 nm using an empirical correction factor of 1.48 (Du et al., 2023). Additionally, the original half-hourly tower-based SIF data were temporally upscaled to daily and monthly values with the aid of PAR and NDVI, following the method described by Hu et al. (2018).

## 3 Results

### 3.1 Downscaled SIF dataset

The comparison of fine-resolution ( $0.05^\circ$ ) and coarse-resolution ( $1^\circ$ ) SIF datasets, derived from GOME, is illustrated in Fig. 2. The top two rows (panels a–f) illustrate the enhanced spatial variability achieved through the downscaling process, revealing finer vegetation patterns and distinct intensity gradients. The downscaled SIF datasets render subtle patterns in SIF more apparent compared to the original coarse-resolution data (panels g–k). Additionally, the downscaling method, which incorporates neighborhood-based pixel searching, effectively fills in data gaps in the original data while preserving spatial continuity. The residual, which was calculated as the difference between the downsampled SIF (which was re-aggregated to the original  $1^\circ$  resolution) and the original SIF, is shown in panels (l)–(p). It can be observed that in major vegetated regions, the residuals are concentrated within the range of  $-0.50$  to  $0.50 \text{ mW m}^{-2} \text{ sr}^{-1} \text{ nm}^{-1}$ . The histograms of the downscaling residuals across different years and sensors are shown in Fig. S2. Overall, the absolute values of the mean residuals are less than  $0.008 \text{ mW m}^{-2} \text{ sr}^{-1} \text{ nm}^{-1}$ , and the standard deviations are below  $0.105 \text{ mW m}^{-2} \text{ sr}^{-1} \text{ nm}^{-1}$ .

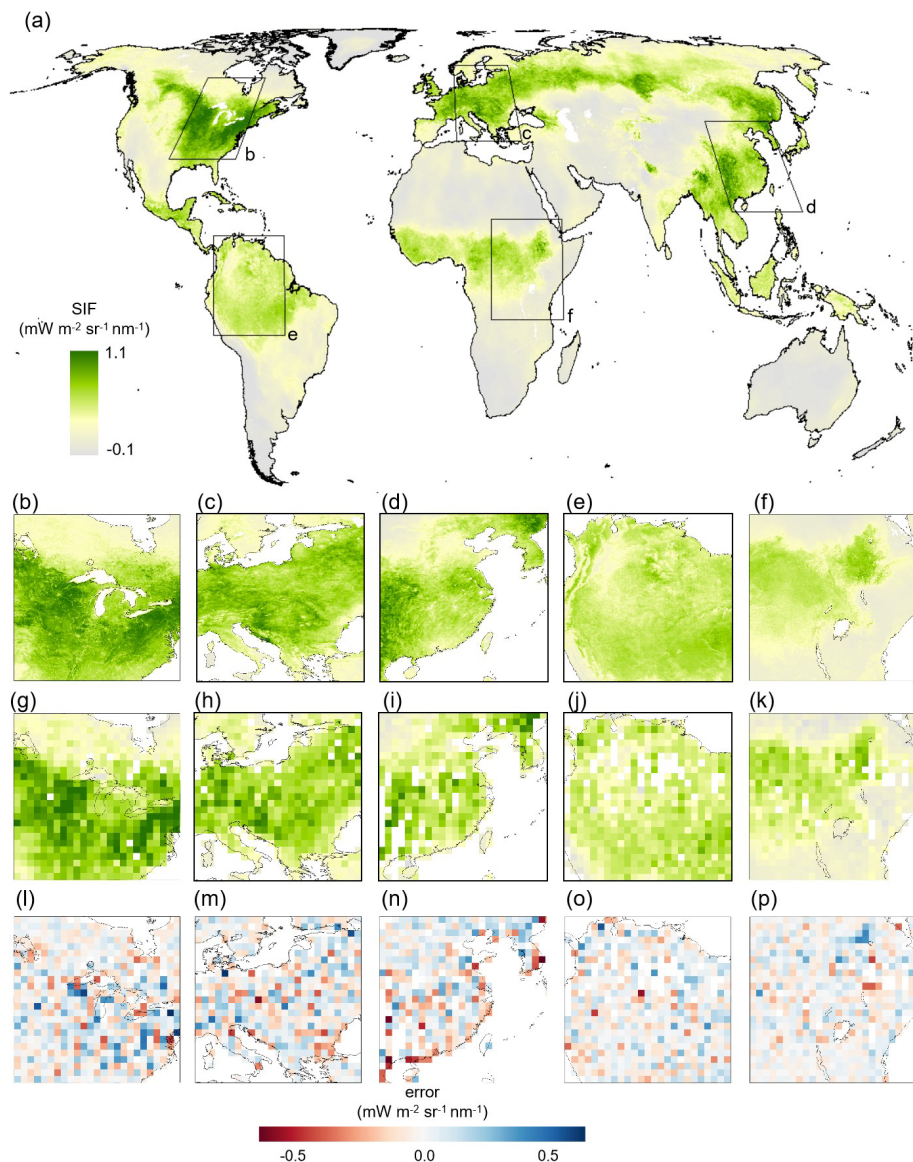


**Figure 2.** Spatially downscaled SIF maps (a–f) compared to the original SIF maps at a coarser resolution (g–k). SIF data from GOME observations in July 1996 are shown as an example. The bottom row (l–p) shows the downscaling residuals, which were calculated as the difference between the original SIF and the downscaled SIF, which was re-aggregated to the original resolution ( $1^\circ \times 1^\circ$ ). Panels (b), (g), and (l) depict North America; (c), (h), and (m) focus on Europe; (d), (i), and (n) depict East Asia (centered on China); (e), (j), and (o) represent the Amazon Basin; and (f), (k), and (p) show Sub-Saharan Africa.

The distribution of monthly SIF before and after spatial downscaling is shown using GOME as an example (Fig. 3), while results for the other three satellites are provided in Figs. S3–S5. The spatially downscaled SIF ( $0.05^\circ \times 0.05^\circ$ ) was re-aggregated to  $1^\circ \times 1^\circ$  or  $0.5^\circ \times 0.5^\circ$  resolution for comparison with the original coarse-resolution SIF. The results demonstrate that the SIF values from the re-aggregated pixels are generally consistent with the original SIF values, closely clustering along the 1 : 1 line and showing strong agreement ( $R^2 > 0.73$ ,  $\text{RMSE} < 0.11 \text{ mW m}^{-2} \text{ sr}^{-1} \text{ nm}^{-1}$ ), indicating that the LUE-based downscaling model effectively

captures the relationship between SIF and its driving variables.

The temporal and spatial distributions of the spatial downscaling residuals were analyzed (Fig. 4). The monthly mean residuals across different latitudes and months were generally below  $0.2 \text{ mW m}^{-2} \text{ sr}^{-1} \text{ nm}^{-1}$  (Fig. 4a). In addition, the regions with relatively larger residuals (e.g.,  $> 0.1 \text{ mW m}^{-2} \text{ sr}^{-1} \text{ nm}^{-1}$ ) were mainly located in high-latitude areas. As shown by the temporally averaged residuals (Fig. 4b), for most areas below  $70^\circ \text{N}$ , the absolute mean residuals are less than  $0.05 \text{ mW m}^{-2} \text{ sr}^{-1} \text{ nm}^{-1}$  for regions

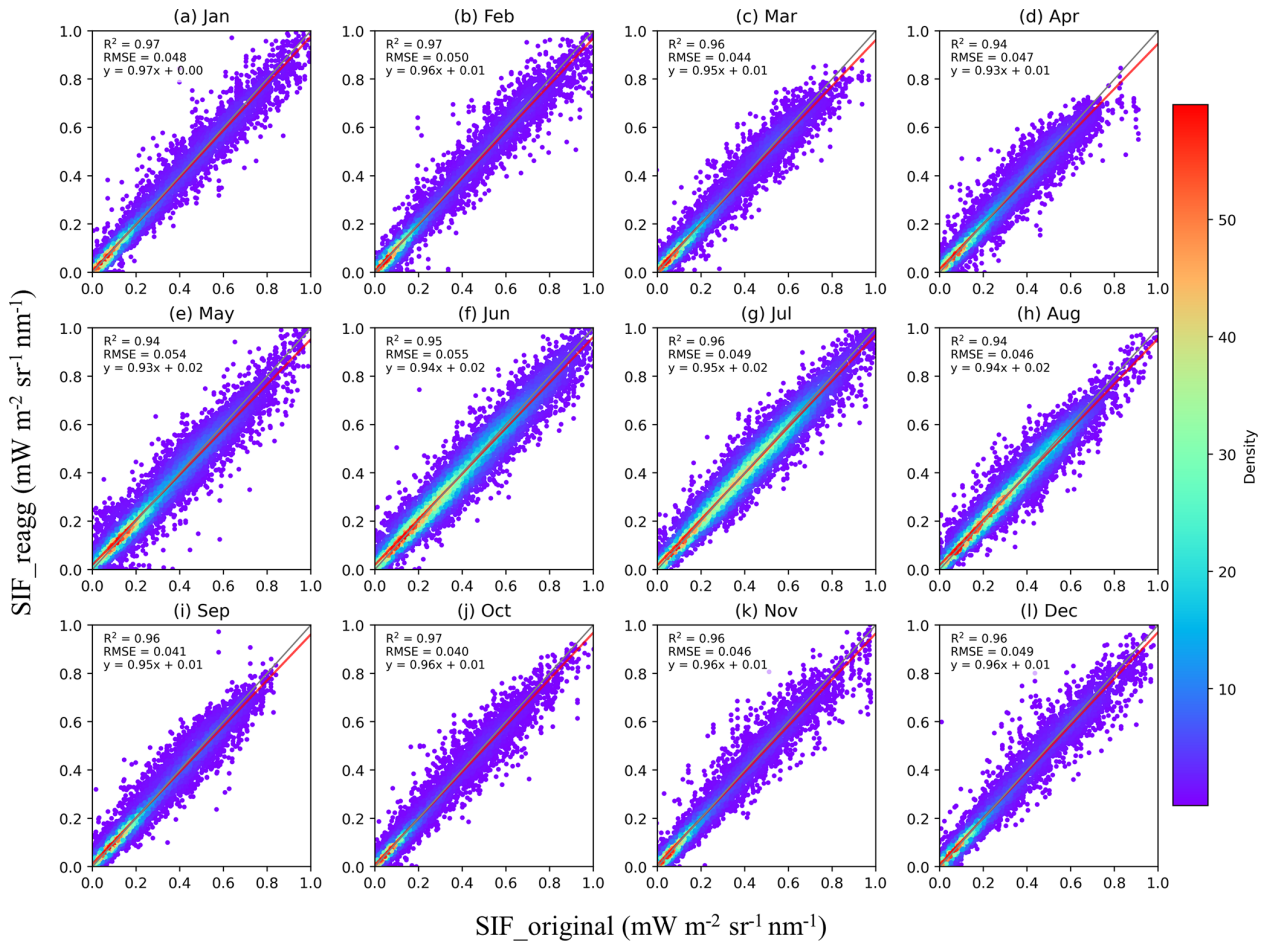


**Figure 3.** The relationship between the reaggregated GOME SIF (SIF\_reagg) and the original GOME SIF (SIF\_original) for 1998 (by month).

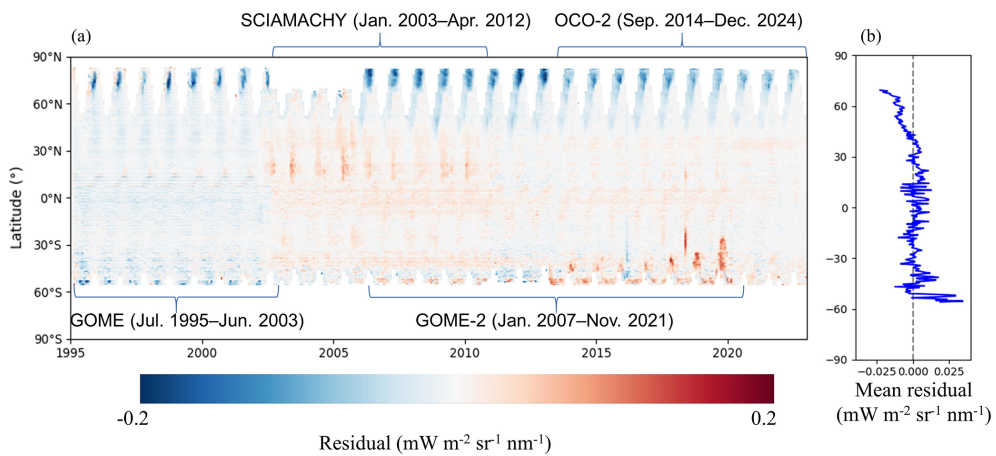


**Figure 4.** The (a) time series and (b) temporal average of the latitudinally distributed residual generated by the LUE-based downscaling model. The residuals are calculated as the difference between the reaggregated SIF (SIF\_reagg) and the original SIF (SIF\_original). For consistency, the coarse spatial resolution SIF datasets were uniformly resampled to  $0.5^\circ \times 0.5^\circ$ . Only data for latitudes below  $70^\circ$  N are shown in (b).

below 70° N. These results indicate that the downscaling method maintains high consistency with the original data across a broad range of temporal and spatial conditions.

### 3.2 Temporal harmonization

The time series of the original SIF datasets from individual satellites and the resulting long-term harmonized SIF dataset (1995–2024) are presented in Fig. 5. Before normalization, substantial inter-sensor discrepancies were observed: mean SIF values ranged from  $0.19 \text{ mW m}^{-2} \text{ sr}^{-1} \text{ nm}^{-1}$  (SCIAMACHY) to  $0.28 \text{ mW m}^{-2} \text{ sr}^{-1} \text{ nm}^{-1}$  (GOME), while interannual trends varied from  $-0.76 \% \text{ yr}^{-1}$  (GOME) to  $0.54 \% \text{ yr}^{-1}$  (GOME-2). Among the original sensor datasets, only the GOME-2 dataset showed a statistically significant trend ( $p < 0.05$ ), whereas other sensors exhibited non-significant variations ( $p \geq 0.05$ ). In contrast, the harmonized LHSIF dataset demonstrated a significant positive trend ( $p < 0.001$ , Trend =  $0.31 \% \text{ yr}^{-1}$ ).

Error analyses were conducted for different climatic zones and plant functional types. Figure 6 shows the comparison between GOME-2 and SCIAMACHY SIF, both before and after normalization. In all tested scenarios, the normalization process substantially reduced the differences between the two sensors. Overall, the MSD decreased by more than 49 % following normalization. In most cases, the difference in the average (bias, shown in red) was the dominant component of the MSD between GOME-2 and SCIAMACHY SIF before normalization. In the temperate and tropical zones of the Southern Hemisphere, discrepancies were primarily attributed to variations in variance (shown in green) and weak correlations (shown in blue). The MSD was reduced after temporal correction, with a decrease in the proportion of bias. Only a small proportion ( $\sim 0.002 \text{ mW m}^{-2} \text{ sr}^{-1} \text{ nm}^{-1}$ ) of phase-related errors remained in the corrected dataset.

The annual maximums of the global-averaged SIF were used to investigate the fluctuation of the worldwide vegetation from 1995 to 2024. Noticeable interannual fluctuations were found for the SIF time series without normalization, with an overall decline (blue line in Fig. 7a). The normalized SIF time series reveals a growth rate of  $0.31 \% \text{ yr}^{-1}$ . After normalization, the standard deviation of the fitted slope decreases from 0.25 % to 0.07 %, indicating a reduction in uncertainty. The boxplot in Fig. 7b further shows a narrower range of SIF values after temporal normalization, suggesting a more concentrated data distribution and improved comparability across sensors.

Significant SIF increases are observed in South and Southeast Asia, as well as parts of Eastern Europe. Conversely, significant declines in SIF are mainly found in Southern Africa and parts of Western North America. In Australia, the eastern regions show slight increases in SIF, while the western regions experience declines. Overall, SIF growth occurred in about 63 % of the world's vegetated areas, with significant

increases observed in around 28 % of these areas between 1996 and 2024 (Fig. 8b).

### 3.3 Validation and comparative analysis

The annual maximum LHSIF exhibited a positive trend ( $0.31 \pm 0.07 \% \text{ yr}^{-1}$ ), with data points clustering around the trendline (Fig. 9a). The growth rate of LHSIF ( $0.31 \% \text{ yr}^{-1}$ ) closely aligns with that of BEPS GPP (Fig. 9f,  $0.47 \% \text{ yr}^{-1}$ ), demonstrating LHSIF's stability in capturing long-term trends of GPP. LT\_SIFc\* also shows a positive trend but with a lower growth rate (Fig. 9b). The SIF\_005 product exhibits a negative trend during 2003–2017 in stark contrast to all other datasets (Fig. 9c). Although the spurious trends have been largely corrected for the original SIF products used by SIF\_005, the long-term trend remains suboptimal.

From 1995 to 2021, less pronounced trends were shown by AVHRR NDVI (Fig. 9d,  $0.18 \pm 0.02 \% \text{ yr}^{-1}$ ) and NIRv (Fig. 9e,  $0.34 \pm 0.02 \% \text{ yr}^{-1}$ ) compared with SIF and GPP. Compared to SIF-based products, NDVI is more susceptible to interference from vegetation canopy structure and non-photosynthetic processes; thus, it is less effective at capturing photosynthetic activity. In this regard, LHSIF provides a more direct indication of photosynthesis and can supplement NDVI and NIRv in detecting changes in GPP.

The interannual trends of several long-term SIF products – including LHSIF, LT\_SIFc\*, SIF\_005, and LCSIF – were compared. The annual maximum of global monthly SIF was used for comparison. Figure 10 presents the results for the global scale as well as for several representative climate zones and land cover types.

Among the four SIF products, all except SIF\_005 show increasing global trends. LHSIF exhibits the strongest upward trend at  $0.31 \% \text{ yr}^{-1}$ , while LCSIF presents the most stable interannual variation, with a trend standard deviation of only  $0.01 \% \text{ yr}^{-1}$ . LHSIF and LCSIF display statistically significant increases on the global scale, whereas the trends for LT\_SIFc\* and SIF\_005 are not statistically significant. The divergent trend between SIF\_005 and the other SIF products is further demonstrated on regional scales. For example, in continental cropland regions (Fig. 10h) and temperate deciduous broadleaf forest (DBF) biomes (Fig. 10e), LHSIF, LT\_SIFc\*, and LCSIF generally exhibit consistent positive trends, whereas SIF\_005 shows a declining trend.

In most cases shown in Fig. 10, LHSIF, LT\_SIFc\*, and LCSIF display consistent trends. An exception occurs in arid regions, where LCSIF shows an increasing trend while both LHSIF and LT\_SIFc\* exhibit decreasing trends (Fig. 10j, k). This divergence may be attributed to the machine learning-based nature of LCSIF, which relies heavily on predictor variables and may not fully capture the actual SIF dynamics under stress conditions. In contrast, the observational basis of LHSIF enables it to more directly reflect regional responses to environmental variability.

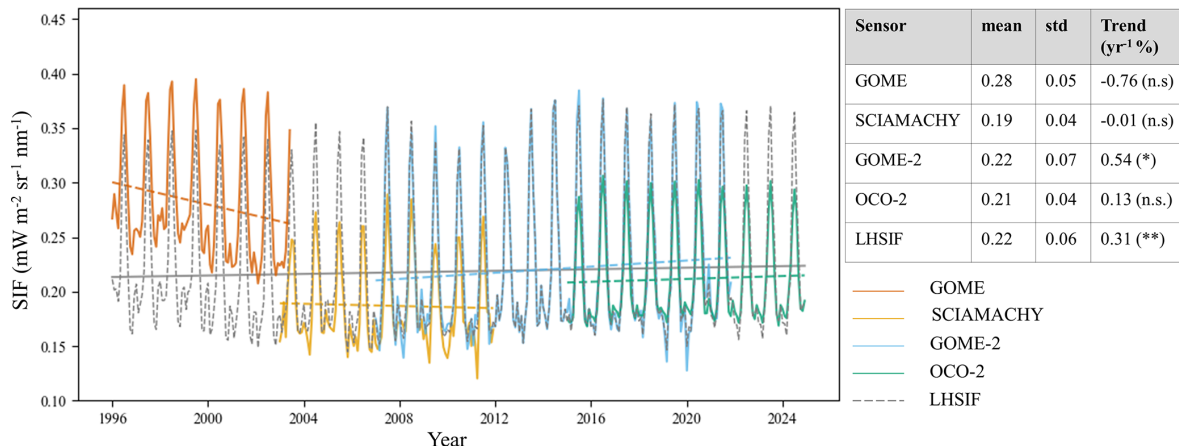


**Figure 5.** Global-averaged SIF time series derived from GOME (yellow), SCIAMACHY (blue), GOME-2 (green), and OCO-2 (red), along with the long-term harmonized SIF time series (LHSIF, gray dotted line), which aligns the satellite datasets based on overlapping periods. The table on the right summarizes the statistical characteristics of each sensor, including the mean, standard deviation (std), and the annual trend (Trend) averaged over the respective periods. The statistical significance of the trends is indicated as follows: n.s. for not significant ( $p \geq 0.05$ ), \* for significant ( $p < 0.05$ ), and \*\* for highly significant ( $p < 0.01$ ).

In addition to long-term satellite products, ground-based observations were also incorporated for comparison. The relationships of LHSIF and AVHRR NDVI with FLUXNET GPP are illustrated in Fig. 11. The LHSIF product shows a strong ability to track GPP, especially for cropland and mixed forest types (Fig. 11a). In contrast, NDVI consistently exhibits lower  $R^2$  values (Fig. 11b) and a more pronounced nonlinear relationship with GPP due to saturation effects. Apart from a few groups in the Southern Hemisphere (such as grasslands in tropical and arid areas), where only a small number of sites are available (see Fig. S1), SIF outperforms NDVI in most cases.

Additionally, comparisons were conducted between LHSIF and the tower-based SIF measurements at five ChinaSpec sites. As a result, LHSIF demonstrated strong agreement with tower-based SIF measurements both temporally and spatially (Fig. 12). The consistency of the intra-annual variations was evident between LHSIF and the in-situ measurements for each site. As shown in the right panel, the monthly composite values are highly correlated, with most points clustering near the 1 : 1 line and correlation coefficients generally exceeding 0.6.

However, some deviations were observed. For example, at the Gucheng (GC) and Xiaotangshan (XTS) sites, which are characterized as wheat-maize rotation croplands, discrepancies occurred in June. During this month, tower-based SIF measurements recorded a trough when wheat was harvested and maize had yet to emerge. Due to spatial heterogeneity, LHSIF was unable to capture this phenomenon, resulting in a reduced correlation between LHSIF and in-situ measurements at these two sites. To highlight the overall correlation, the data in June for these two sites were removed from the scatter plot (Fig. 12h, j).

## 4 Discussion

### 4.1 Improvements in cross-sensor harmonization

In this study, we applied a CDF normalization method to harmonize cross-sensor SIF measurements. While the general concept and algorithm are similar to previous studies (Wen et al., 2020; Wang et al., 2022), our data processing framework incorporates several key improvements.

Firstly, a temporally corrected GOME-2A SIF (TCSIF) dataset (Zou et al., 2024) was used as the reference baseline. The TCSIF product incorporates radiometric correction of GOME-2A sensor degradation using a pseudo-invariant method and underwent a two-step validation at both radiance and SIF levels. As shown in Zou et al. (2024), the interannual variability of TCSIF shows strong consistency with GPP, providing a more robust reference for long-term harmonization. In contrast, the SIF\_005 dataset (Wen et al., 2020), which was based on the original GOME-2 SIF, shows pronounced interannual fluctuations and a declining trend over 2003–2017, likely due to residual degradation effects (see Figs. 9c and 10).

Secondly, our harmonization strategy uses GOME-2A as the reference sensor. Its extended data record (2007–2021) provides over five years of overlap with both SCIAMACHY and OCO-2, allowing single-step normalization for each sensor and reducing the uncertainty propagation associated with multi-step corrections. In contrast, the LT\_SIFc\* product uses GOME as the benchmark, relying on only a six-month overlap with SCIAMACHY and then sequentially calibrating SCIAMACHY and GOME-2A, which may accumulate uncertainties.

To quantify the impact of overlap duration on harmonization uncertainty, we performed normalization experi-

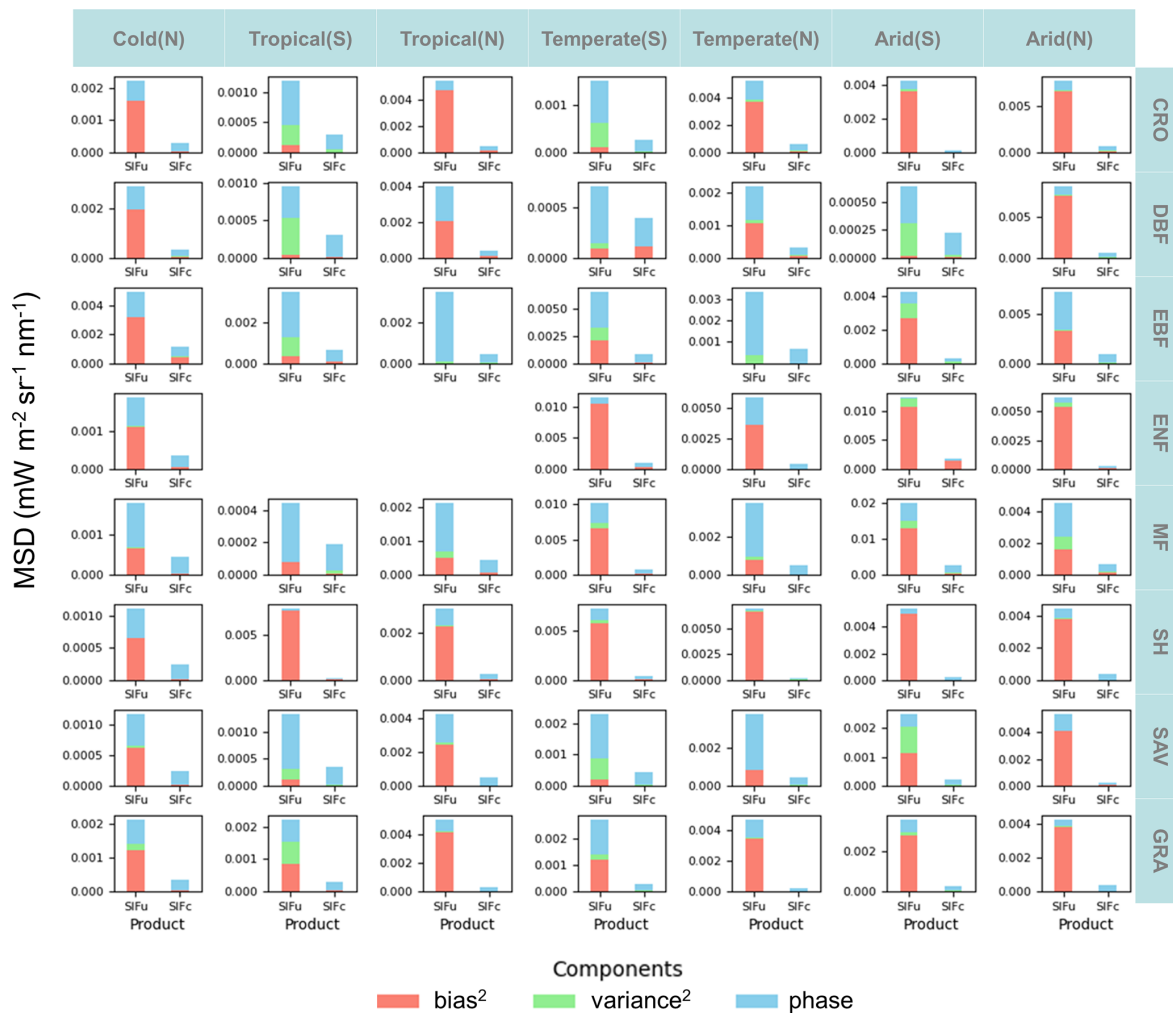


**Figure 6.** The mean squared difference (MSD) between GOME-2 SIF and SCIAMACHY SIF before ( $SIF_u$ ) and after ( $SIF_c$ ) normalization. The results show the average conditions across different climatic zones and vegetation functional categories during 2007.

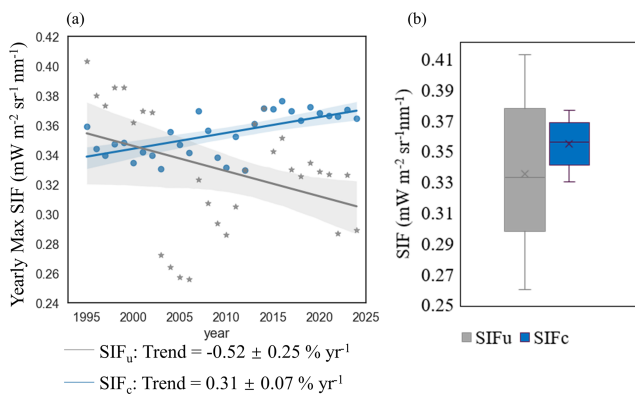


**Figure 7.** (a) Trend and (b) box plot of the yearly maximum global-averaged SIF of the combined time series before ( $SIF_u$ ) and after ( $SIF_c$ ) normalization during 1995–2024.

ments using 6-, 12-, and 24-month overlap periods between GOME-2 and SCIAMACHY/OCO-2, each experiment was repeated 10 times to assess the variability (Fig. 13).

The results show that a six-month overlap leads to a higher standard deviation in SIF time series compared to longer overlaps. As the overlap period was extended from 6 to 12 months, the standard deviations of the normalized SIF series decreased from  $0.015$  to  $0.007 \text{ mW m}^{-2} \text{ sr}^{-1} \text{ nm}^{-1}$  (SCIAMACHY) and from  $0.018$  to  $0.005 \text{ mW m}^{-2} \text{ sr}^{-1} \text{ nm}^{-1}$  (OCO-2), representing a reduction of over 53.3 %. These results confirm that short overlap periods increase normalization uncertainty and highlight the robustness of our chosen strategy, which avoids using GOME as the baseline. Besides, the early-stage LHSIF exhibits stronger consistency with data-driven LCSIF than LT\_SIFc\* (Fig. 10a), providing additional support for its early-period reliability.

Furthermore, in contrast to the pixel-by-pixel matching methods adopted in previous studies, we applied a region-

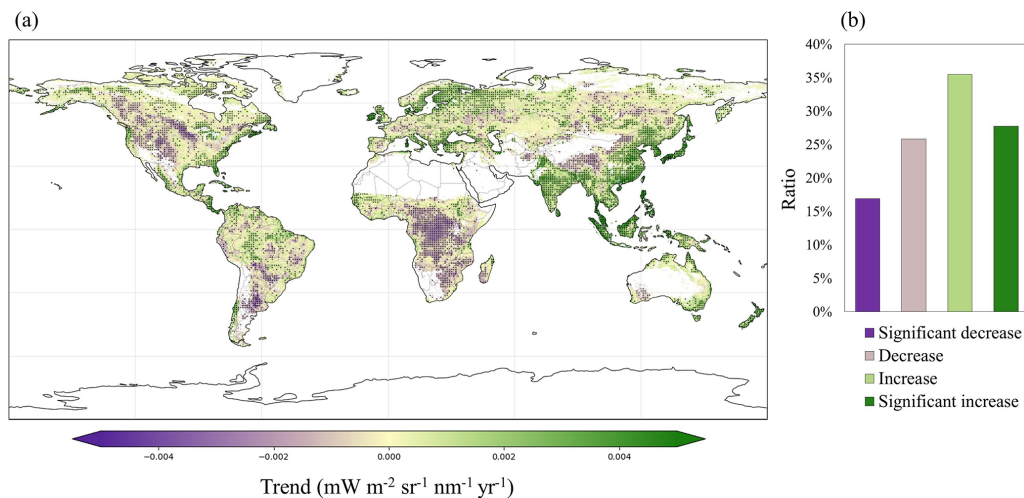


**Figure 8.** (a) Map of trends in LHSIF for 1996–2024. (b) Percentage of areas in global vegetation covered by four different trend types (significant decrease: negative correlation and  $p < 0.05$ ; decrease: negative correlation and  $p \geq 0.05$ ; increase: positive correlation and  $p \geq 0.05$ ; and significant increase: positive correlation and  $p < 0.05$ ). The black dots in (a) represent statistically significant trends ( $p < 0.05$ ). The statistics begin in 1996 due to incomplete data coverage in 1995, which only includes the second half of the year (July–December).

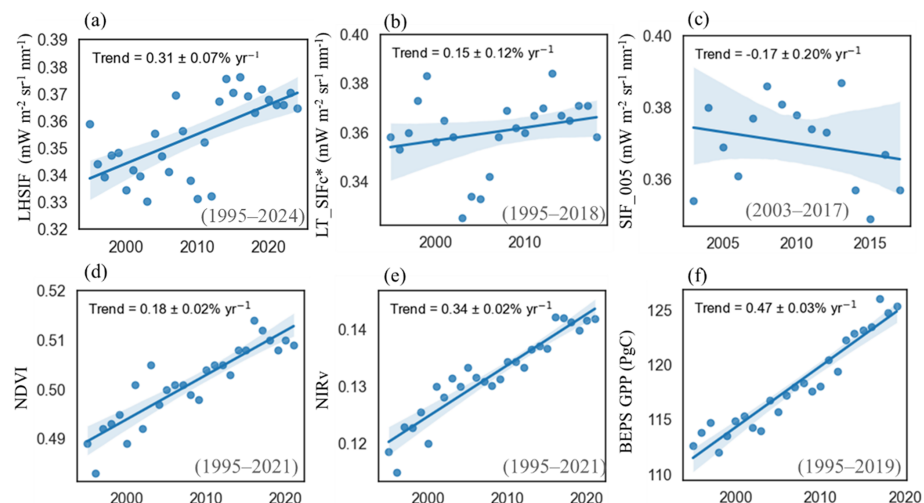


**Figure 9.** The yearly maximum (a) LHSIF compared with (b) LT\_SIFc\*, (c) SIF\_005, (d) AVHRR NDVI, (e) AVHRR NIRv, as well as the annual total (f) BEPS GPP. See Table 2 for dataset details.

based and month-specific normalization strategy. The region-based approach allows for a larger sample size within each region, potentially enabling an improved estimation of the CDF, while the month-specific treatment helps account for seasonal variations in the CDF. The improved stability of interannual trends in the LHSIF product, compared to LT\_SIFc\* and SIF\_005 at both global and regional scales (Fig. 10), appears to reflect the effects of this normalization strategy.

#### 4.2 Limitations and future perspectives

Our investigation shows that the CDF normalization approach effectively reduces disparities across sensors, providing a unified reference framework with the longest time series to date. While the normalized dataset exhibits consistent seasonal and interannual patterns across sensors, several methodological considerations warrant discussion. First, as a statistical approach distinct from physical calibration methods (e.g., pseudo-invariant target radiometry), CDF matching may retain minor sensor-specific biases. Second, although we incorporate annual land cover updates using MCD12C1 product to account for vegetation dynamics, inherent classification uncertainties in the reference dataset persist. Nev-

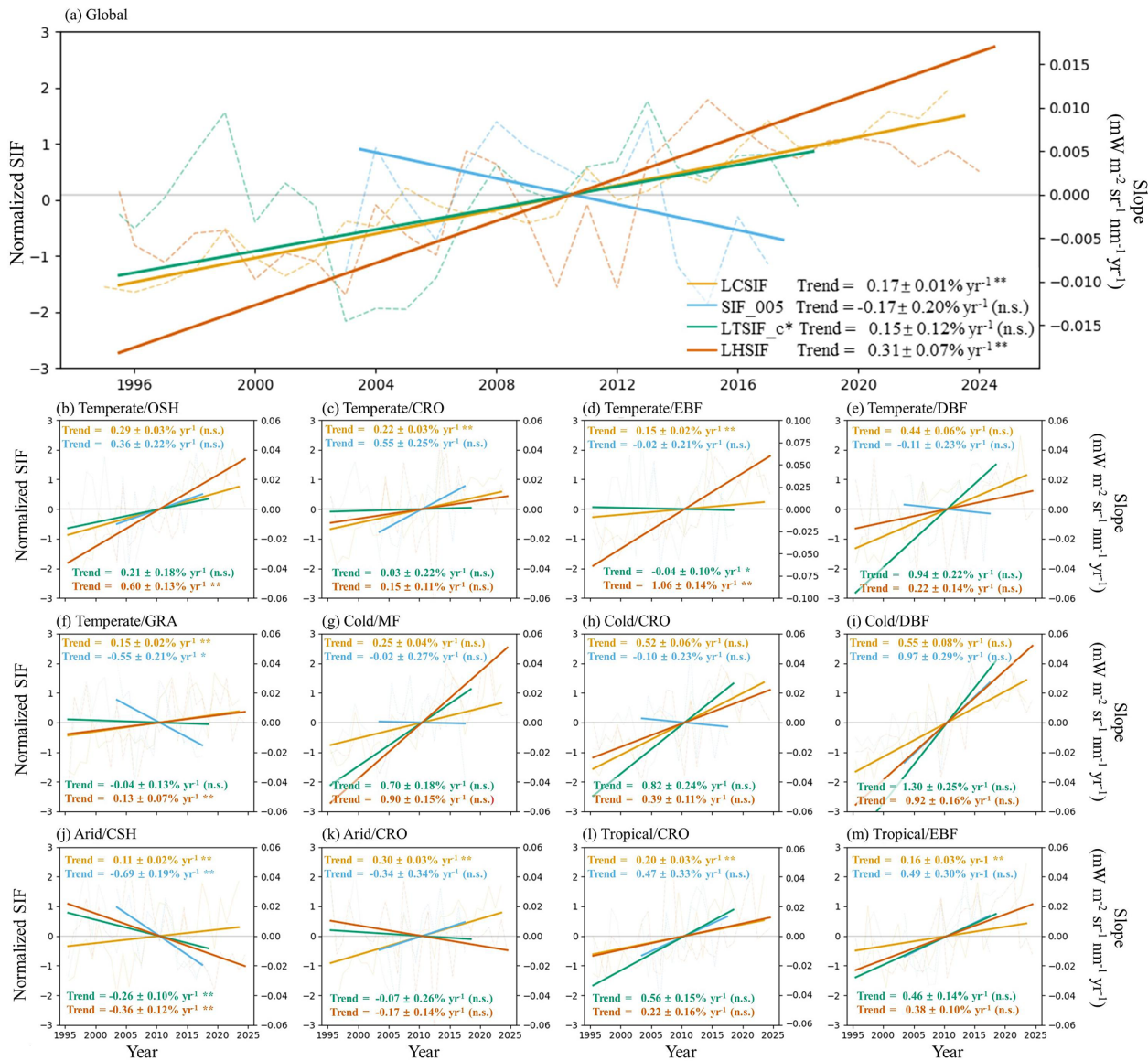


**Figure 10.** Comparison of interannual variations in long-term SIF products. LHSIF (red), LT\_SIFc\* (green), SIF\_005 (purple), and LCSIF (blue) are compared for **(a)** the global scale and **(b–m)** various climatic and vegetation regions. All datasets were normalized using the  $z$ -score method. Dashed lines represent yearly maximum values, and solid lines indicate linear trends. To aid visual comparison, trend lines were anchored at the origin (2010, 0). The statistical significance of the trends is indicated as follows: n.s. for not significant ( $p \geq 0.05$ ), \* for significant ( $p < 0.05$ ), and \*\* for highly significant ( $p < 0.01$ ). See Table 2 for dataset details.

ertheless, the percentile-based CDF matching demonstrates inherent robustness against outliers (Wang et al., 2022), rendering land cover-induced biases negligible in practice. The most robust approach for cross-sensor calibration is based on pseudo-invariant calibration sites (PICs) located in non-vegetated areas (Markham and Helder, 2012; Khakurel et al., 2021). This method has been successfully applied to the normalization and long-term monitoring of reflectance data and vegetation index products (Angal et al., 2013; Mishra et al., 2014; Jeong et al., 2024; Tavora et al., 2023). However, in commonly used PICs, such as deserts and water surfaces, SIF

signals are inherently weak and highly susceptible to noise that can cause significant uncertainty in PIC-based calibration for SIF applications.

Although the normalization method was designed to minimize the influence of GOME-related uncertainties on the harmonized dataset, the accuracy of early LHSIF data (1995–2003) still warrants cautious interpretation. Additional analyses were conducted for the GOME observation period. Despite the brief overlap with SCIAMACHY, the two datasets showed broadly consistent seasonal dynamics (Fig. 14a). We further compared the temporal trends of LHSIF, LCSIF, and

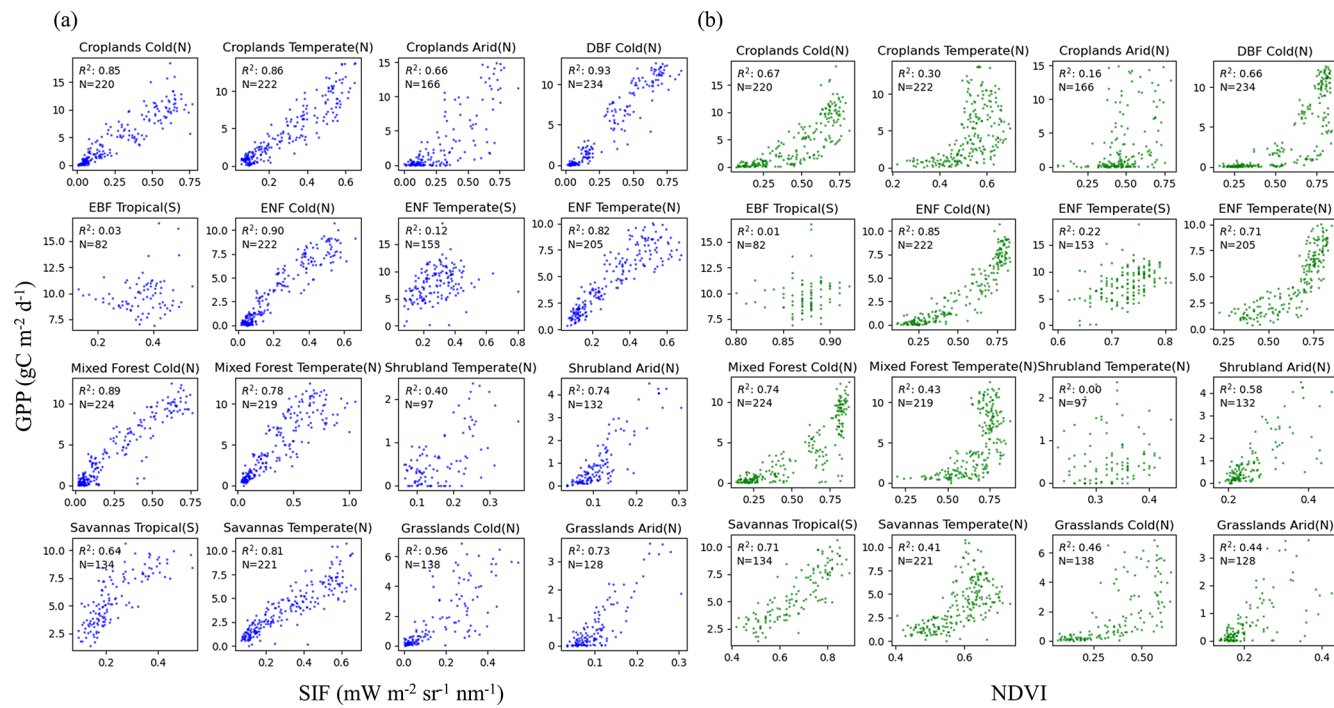


**Figure 11.** Comparison of long-term relationships between SIF vs. GPP and NDVI vs. GPP at FLUXNET sites. Only those flux tower sites that have accumulated over a decade of data were chosen and subsequently categorized according to their respective climate zones and vegetation types.

AVHRR NDVI during 1995–2003 (Fig. 14b–d). Some regions, such as western Europe, northern Oceania, and the southern parts of both North and South America, showed broadly consistent increasing trends across datasets. Conversely, declines were commonly observed in central Africa, southern Oceania, the Amazon rainforest, and northwestern India. Nevertheless, noticeable discrepancies remain. For instance, LHSIF displayed more extensive declines in high-latitude regions and central North America, which were not consistently captured by either LCSIF or NDVI.

These inconsistencies may reflect several limitations of the early GOME record, including (i) the coarse spatial resolution that amplifies mixed-pixel effects (Joiner et al., 2013), (ii) the relatively low signal-to-noise ratio of the GOME instrument (Burrows et al., 1999), (iii) increased retrieval uncertainties in high-latitude regions with low fluorescence intensity (Köhler et al., 2015), and (iv) potential uncorrected sensor degradation effects. As our harmonization approach primarily reduces inter-sensor biases through normalization, it cannot fundamentally resolve these intrinsic limitations of the original GOME data. In addition, errors may also arise from the propagation and accumulation of uncertainties during the normalization process, since GOME was further adjusted based on the corrected SCIAMACHY product.

Future work will require dedicated strategies to address the intrinsic limitations of early GOME observations. Such strategies may include radiometric recalibration using

pseudo-invariant sites (Zou et al., 2024) and also physically-based harmonization approaches to mitigate sensor inconsistencies arising from observation geometry, atmospheric conditions, pixel size, and background signals. Implementing these approaches will enhance the reliability of early trends, providing a more robust foundation for interpreting long-term variations in satellite-observed SIF.

Additionally, our downscaling approach follows the methodology proposed by Duveiller and Cescatti (2016) and Duveiller et al. (2020), where NIRv is used in the LUE model instead of NDVI to enhance the model's interpretability for SIF (Badgley et al., 2017). Nevertheless, some explanatory variables remain unaccounted for. For instance, incorporating PAR could improve model interpretability under cloudy conditions (Ryu et al., 2018). However, discrepancies in overpass time and scale effects can cause inconsistencies between PAR and SIF products, which may increase uncertainties in the downscaling model. Furthermore, incorporating fluorescence escape efficiency (Ryu et al., 2019) and topographic factors (Chen et al., 2022; Tao et al., 2024) into the downscaling model could further enhance its performance.

Model selection is ultimately more critical than the choice of input variables (Duveiller et al., 2020). Previous research on spatial downscaling was predominantly using purely empirical machine-learning approaches (Gentine and Aleommah, 2018; Wen et al., 2020; Hong et al., 2022; Lu et al., 2024). An alternative strategy redistributes the initial global

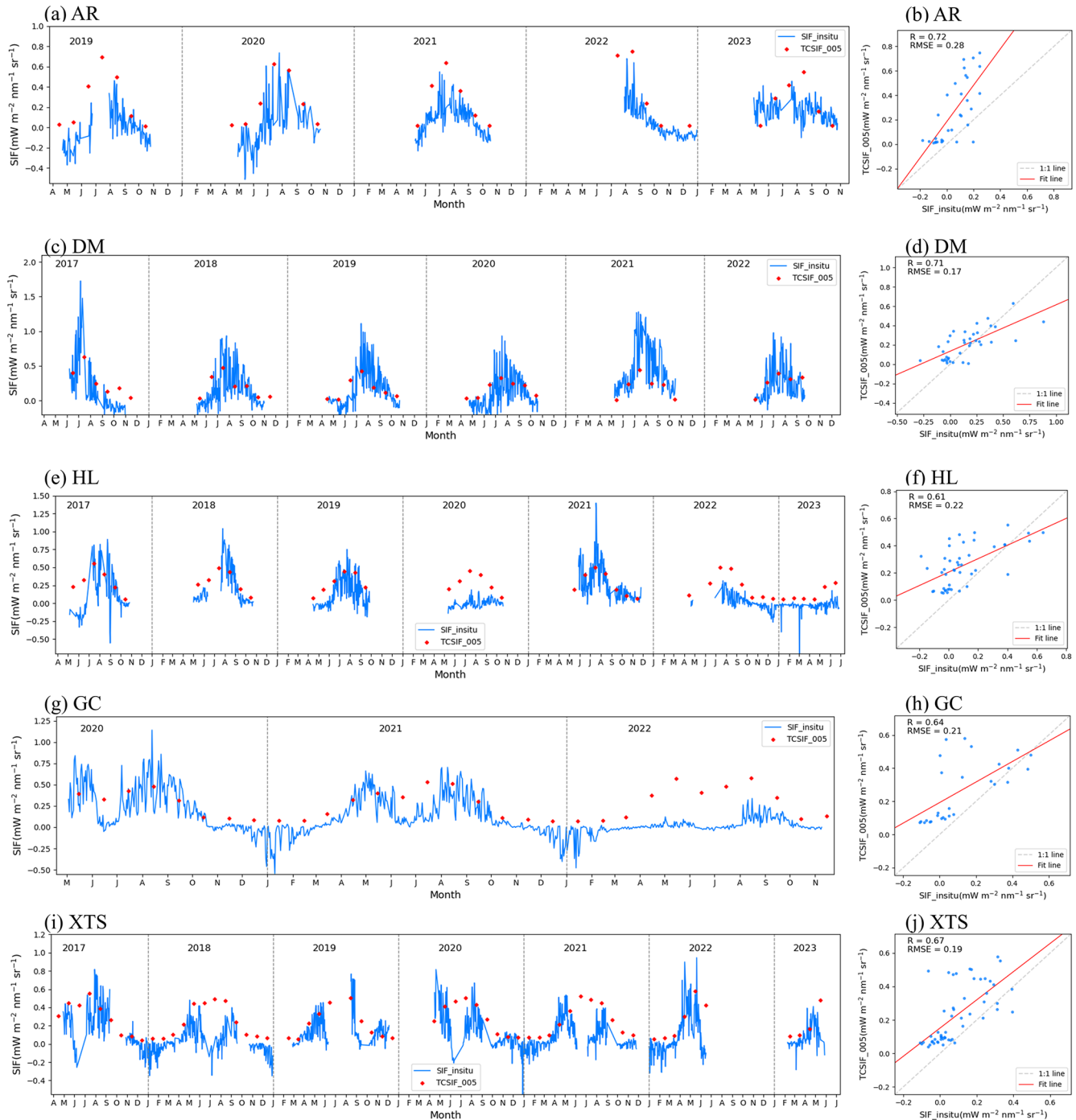


**Figure 12.** Comparison between LHSIF with the tower-based SIF measurements (SIF\_institu) at (a, b) AR, (c, d) DM, (e, f) HL, (g, h) GC, and (i, j) XTS sites. The temporal pattern of LHSIF compared with daily and monthly averaged SIF\_institu is shown in the left and right columns. The horizontal axis of the chart in the left column represents the first letters of the month names. Data points in June were excluded from the scatter plot for GC and XTS (h, j).

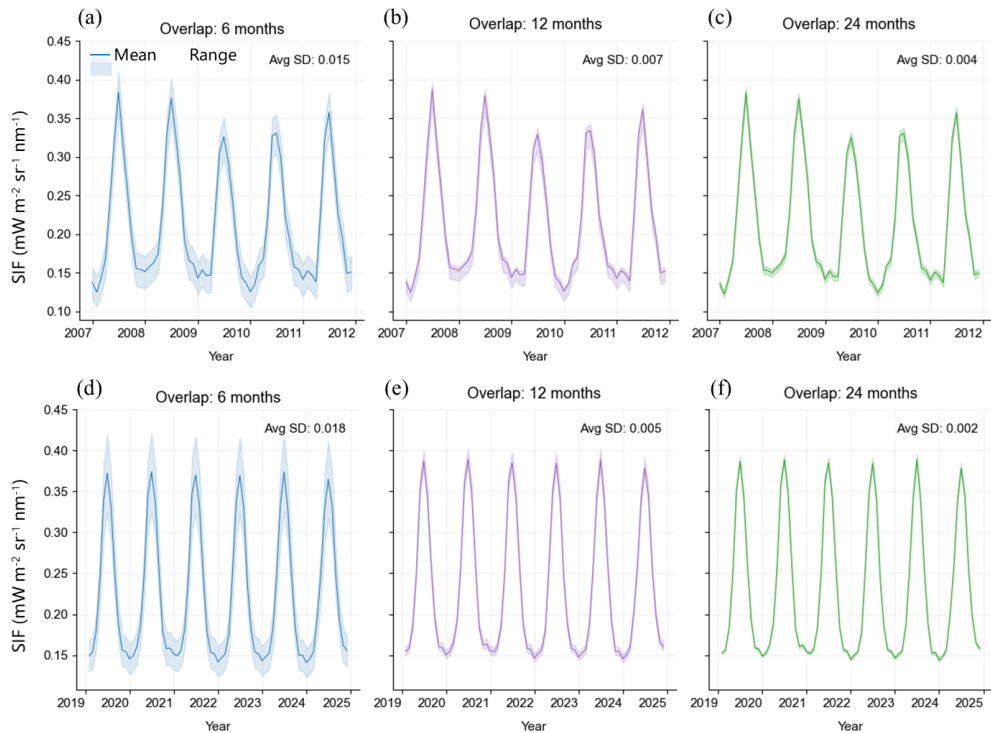


**Figure 13.** Normalized SIF time series using different overlap durations: 6 months (first column), 12 months (second column), and 24 months (third column) from SCIAMACHY (top row) and OCO-2 (bottom row). The shaded areas represent the standard deviation (SD) across multiple experiments, with units of  $\text{mW m}^{-2} \text{sr}^{-1} \text{nm}^{-1}$ .

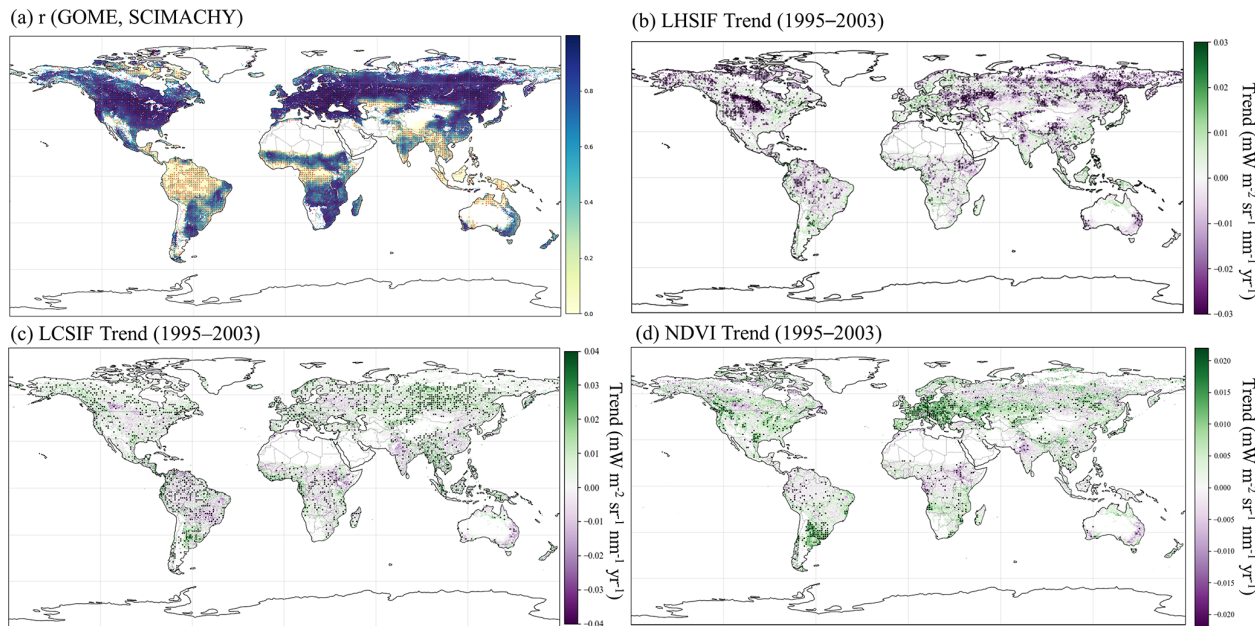


**Figure 14.** Comparisons of GOME SIF, SCIAMACHY SIF, LHSIF, LCSIF, and AVHRR NDVI during 1995–2003. (a) Correlation coefficient between GOME and SCIAMACHY SIF time series; annual trends of (b) LHSIF, (c) LCSIF, and (d) AVHRR NDVI. The scatter points represent statistical significance ( $p < 0.05$ ).

downscaling results based on the original coarse-resolution SIF values and retains the characteristics of the original observational signal to the greatest extent possible (Ma et al., 2022; Chen et al., 2025). Our experimental results confirm that our downscaled SIF products also remain consistent with the original signals (Fig. 4). In addition, the LUE-based approach incorporates physiological constraints, ensuring that the downscaled SIF values remain within a reasonable range compared to traditional machine-learning models.

Another type of long-term SIF datasets have been generated by temporally extrapolating SIF observations based on machine-learning methods. These datasets provide more than two decades of high-temporal-resolution data beyond the monthly scale (Zhang et al., 2018b; Li and Xiao, 2019; Fang et al., 2023). However, such datasets predominantly depend on model-driven predictions constrained by satellite observation periods, rather than being based on actual observational data, which is fundamentally different from the approach we employed here (Chen et al., 2025; Ma et al., 2022).

Previous findings have demonstrated that satellite-observed SIF is capable of capturing ecosystem responses to major climatic extremes, such as the suppression of photosynthesis during the 2015/16 El Niño event in the tropics and drought-induced declines in Europe and North America (Shekhar et al., 2020; Sun et al., 2015; Yoshida et al., 2015). These findings provide support for the potential advantages of LHSIF in reflecting regional environmental variability. Nevertheless, detailed attribution of interannual differences among products to specific climatic events requires dedicated analyses and applications, which should be pursued in future work.

Currently, the temporal resolution of purely observation-based enhanced SIF products that span longer than 20 years remains constrained at the monthly scale, largely due to noise in the satellite SIF products. Overcoming this limitation will require further refinement of existing downscaling models, paving the way for future products to achieve a resolution of 16 d or higher.

## 5 Data availability

The LHSIF dataset generated in this study is publicly available at <https://doi.org/10.5281/zenodo.16394372> (Zou et al., 2025). Additional information regarding the data and methods is available upon request from the corresponding author.

## 6 Conclusion

In this study, we developed a long-term harmonized SIF dataset (LHSIF) spanning 1995 to 2024. SIF datasets from various satellites were normalized using multi-sensor SIF observations through a CDF normalization approach, using the temporally corrected GOME-2A SIF dataset as a bench-

mark. An LUE-based model was used for spatial downscaling, yielding a fine resolution of  $0.05^\circ$  with an absolute mean residual less than  $0.05 \text{ mW m}^{-2} \text{ sr}^{-1} \text{ nm}^{-1}$ .

Our analysis demonstrated that the harmonized dataset reduced overall errors by more than 49 % and exhibited a stable interannual increase ( $0.31 \pm 0.07 \% \text{ yr}^{-1}$ ). The interannual trend of LHSIF closely aligns with the growth of GPP ( $0.47 \pm 0.03 \% \text{ yr}^{-1}$ ) and demonstrates superior temporal and spatial consistency compared to NDVI. Validation against ground-based SIF observations ( $R > 0.6$ ) further underscores the reliability of the harmonization approach and the dataset's utility in global vegetation studies.

By focusing on the harmonization of satellite-derived SIF products, the LHSIF dataset offers a unified framework for integrating multi-sensor SIF data to enable long-term monitoring of global photosynthesis. This contribution provides an essential tool for understanding vegetation responses to environmental changes and advancing the field of Earth system science.

**Supplement.** The supplement related to this article is available online at <https://doi.org/10.5194/essd-18-55-2026-supplement>.

**Author contributions.** CZ and LL designed the experiments, CZ carried them out. CZ, SD and XL developed the model code and generated the products. CZ prepared the manuscript with contributions from all co-workers.

**Competing interests.** The contact author has declared that none of the authors has any competing interests.

**Disclaimer.** Publisher's note: Copernicus Publications remains neutral with regard to jurisdictional claims made in the text, published maps, institutional affiliations, or any other geographical representation in this paper. While Copernicus Publications makes every effort to include appropriate place names, the final responsibility lies with the authors. Views expressed in the text are those of the authors and do not necessarily reflect the views of the publisher.

**Acknowledgements.** We thank the editors and reviewers for their insightful comments. This study utilized the BEPS GPP dataset from the National Ecosystem Science Data Center of China (<http://www.nesdc.org.cn> (last access: 20 October 2025).

**Financial support.** This work was supported by the National Natural Science Foundation of China (grant no. 42425001) and the State Key Laboratory of Efficient Utilization of Arable Land in China (grant no. G2025-05-32).

**Review statement.** This paper was edited by Han Ma and reviewed by Qiaoli Wu and one anonymous referee.

## References

Abatzoglou, J. T., Dobrowski, S. Z., Parks, S. A., and Hegewisch, K. C.: TerraClimate, a high-resolution global dataset of monthly climate and climatic water balance from 1958–2015, *Scientific Data*, 5, 170191, <https://doi.org/10.1038/sdata.2017.191>, 2018.

Anav, A., Friedlingstein, P., Beer, C., Ciais, P., Harper, A., Jones, C., Murray-Tortarolo, G., Papale, D., Parazoo, N. C., Peylin, P., Piao, S., Sitch, S., Viovy, N., Wiltshire, A., and Zhao, M.: Spatiotemporal patterns of terrestrial gross primary production: A review, *Reviews of Geophysics*, 53, 785–818, <https://doi.org/10.1002/2015RG000483>, 2015.

Angal, A., Xiong, X., Choi, T., Chander, G., Mishra, N., and Helder, D. L.: Impact of Terra MODIS Collection 6 on long-term trending comparisons with Landsat 7 ETM+ reflective solar bands, *Remote sensing letters*, 4, 873–881, 2013.

Bacour, C., Maignan, F., Peylin, P., MacBean, N., Basnrikov, V., Joiner, J., Köhler, P., Guanter, L., and Frankenberg, C.: Differences Between OCO-2 and GOME-2 SIF Products From a Model-Data Fusion Perspective, *Journal of Geophysical Research: Biogeosciences*, 124, 3143–3157, <https://doi.org/10.1029/2018JG004938>, 2019.

Badgley, G., Field, C. B., and Berry, J. A.: Canopy near-infrared reflectance and terrestrial photosynthesis, *Science Advances*, 3, e1602244, <https://doi.org/10.1126/sciadv.1602244>, 2017.

Beck, H. E., McVicar, T. R., Vergopolan, N., Berg, A., Lutsko, N. J., Dufour, A., Zeng, Z., Jiang, X., van Dijk, A. I. J. M., and Miralles, D. G.: High-resolution (1 km) Köppen-Geiger maps for 1901–2099 based on constrained CMIP6 projections, *Scientific Data*, 10, 724, <https://doi.org/10.1038/s41597-023-02549-6>, 2023.

Beer, C., Reichstein, M., Tomelleri, E., Ciais, P., Jung, M., Carvalhais, N., Rödenbeck, C., Arain, M. A., Baldocchi, D., Bonan, G. B., Bondeau, A., Cescatti, A., Lasslop, G., Lindroth, A., Lomas, M., Luyssaert, S., Margolis, H., Oleson, K. W., Rouspard, O., Veenendaal, E., Viovy, N., Williams, C., Woodward, F. I., and Papale, D.: Terrestrial Gross Carbon Dioxide Uptake: Global Distribution and Covariation with Climate, *Science*, 329, 834–838, <https://doi.org/10.1126/science.1184984>, 2010.

Berry, J. A., Frankenberg, C., Wennberg, P., Baker, I., Bowman, K. W., Castro-Contreras, S., Cendrero-Mateo, M. P., Damm, A., Drewry, D., and Ehlmann, B.: New methods for measurement of photosynthesis from space, *Geophys. Res. Lett.*, 38, L17706, <https://doi.org/10.26206/9NJP-CG56>, 2012.

Burrows, J. P., Weber, M., Buchwitz, M., Rozanov, V., Ladstätter-Weißenmayer, A., Richter, A., DeBeek, R., Hoogen, R., Bramstedt, K., Eichmann, K.-U., Eisinger, M., and Perner, D.: The Global Ozone Monitoring Experiment (GOME): Mission Concept and First Scientific Results, *Journal of the Atmospheric Sciences*, 56, 151–175, [https://doi.org/10.1175/1520-0469\(1999\)056<0151:TGOME>2.0.CO;2](https://doi.org/10.1175/1520-0469(1999)056<0151:TGOME>2.0.CO;2), 1999.

Byrd, R. H., Lu, P., Nocedal, J., and Zhu, C.: A Limited Memory Algorithm for Bound Constrained Optimization, *SIAM Journal on Scientific Computing*, 16, 1190–1208, <https://doi.org/10.1137/0916069>, 1995.

Chen, R., Liu, L., Liu, X., and Rascher, U.: CMLR: A Mechanistic Global GPP Dataset Derived from TROPOMIS SIF Observations, *Journal of Remote Sensing*, 4, 0127, <https://doi.org/10.34133/remotesensing.0127>, 2024.

Chen, S., Liu, L., Sui, L., Liu, X., and Ma, Y.: An improved spatially downscaled solar-induced chlorophyll fluorescence dataset from the TROPOMI product, *Scientific Data*, 12, 135, <https://doi.org/10.1080/22797254.2022.2028579>, 2025.

Chen, X., Huang, Y., Nie, C., Zhang, S., Wang, G., Chen, S., and Chen, Z.: A long-term reconstructed TROPOMI solar-induced fluorescence dataset using machine learning algorithms, *Scientific Data*, 9, 427, <https://doi.org/10.1038/s41597-022-01520-1>, 2022.

Damm, A., Guanter, L., Paul-Limoges, E., van der Tol, C., Hueni, A., Buchmann, N., Eugster, W., Ammann, C., and Schaeppman, M. E.: Far-red sun-induced chlorophyll fluorescence shows ecosystem-specific relationships to gross primary production: An assessment based on observational and modeling approaches, *Remote Sensing of Environment*, 166, 91–105, <https://doi.org/10.1016/j.rse.2015.06.004>, 2015.

Du, S., Liu, X., Chen, J., Duan, W., and Liu, L.: Addressing validation challenges for TROPOMI solar-induced chlorophyll fluorescence products using tower-based measurements and an NIRv-scaled approach, *Remote Sensing of Environment*, 290, 113547, <https://doi.org/10.1016/j.rse.2023.113547>, 2023.

Duveiller, G. and Cescatti, A.: Spatially downscaling sun-induced chlorophyll fluorescence leads to an improved temporal correlation with gross primary productivity, *Remote Sensing of Environment*, 182, 72–89, <https://doi.org/10.1016/j.rse.2016.04.027>, 2016.

Duveiller, G., Filippini, F., Walther, S., Köhler, P., Frankenberg, C., Guanter, L., and Cescatti, A.: A spatially downscaled sun-induced fluorescence global product for enhanced monitoring of vegetation productivity, *Earth Syst. Sci. Data*, 12, 1101–1116, <https://doi.org/10.5194/essd-12-1101-2020>, 2020.

Fang, J., Lian, X., Ryu, Y., Jeong, S., Jiang, C., and Gentine, P.: Reconstruction of a long-term spatially contiguous solar-induced fluorescence (LCSIF) over 1982–2022, *arXiv [preprint]*, <https://doi.org/10.48550/arXiv.2311.14987>, 2023.

Frankenberg, C., Fisher, J. B., Worden, J., Badgley, G., Saatchi, S. S., Lee, J.-E., Toon, G. C., Butz, A., Jung, M., Kuze, A., and Yokota, T.: New global observations of the terrestrial carbon cycle from GOSAT: Patterns of plant fluorescence with gross primary productivity, *Geophysical Research Letters*, 38, <https://doi.org/10.1029/2011GL048738>, 2011.

Friedl, M. and Sulla-Menashe, D.: MODIS/Terra+ Aqua land cover type yearly L3 Global 0.05 Deg CMG V061, NASA EOSDIS Land Processes Distributed Active Archive Center (DAAC) [data set], <https://doi.org/10.5067/MODIS/MCD12C1.061>, 2022.

Gentine, P. and Alemohammad, S. H.: Reconstructed Solar-Induced Fluorescence: A Machine Learning Vegetation Product Based on MODIS Surface Reflectance to Reproduce GOME-2 Solar-Induced Fluorescence, *Geophysical Research Letters*, 45, 3136–3146, <https://doi.org/10.1002/2017GL076294>, 2018.

Guanter, L., Frankenberg, C., Dudhia, A., Lewis, P. E., Gómez-Dans, J., Kuze, A., Suto, H., and Grainger, R. G.: Retrieval and global assessment of terrestrial chlorophyll fluorescence from GOSAT space measurements, *Remote Sensing of Environment*, 121, 236–251, <https://doi.org/10.1016/j.rse.2012.02.006>, 2012.

Guanter, L., Zhang, Y., Jung, M., Joiner, J., Voigt, M., Berry, J. A., Frankenberg, C., Huete, A. R., Zarco-Tejada, P., Lee, J. E., Moran, M. S., Ponce-Campos, G., Beer, C., Camps-Valls, G., Buchmann, N., Ganelle, D., Klumpp, K., Cescatti, A., Baker, J. M., and Griffis, T. J.: Global and time-resolved monitoring of crop photosynthesis with chlorophyll fluorescence, *Proc. Natl. Acad. Sci. USA*, 111, E1327–1333, <https://doi.org/10.1073/pnas.1320008111>, 2014.

Hahne, A., Lefebvre, A., and Callies, J.: Global ozone monitoring experiment on board ERS-2, *Environmental Sensing '92*, SPIE, <https://doi.org/10.1117/12.140233>, 1993.

Hong, Z., Hu, Y., Cui, C., Yang, X., Tao, C., Luo, W., Zhang, W., Li, L., and Meng, L.: An Operational Downscaling Method of Solar-Induced Chlorophyll Fluorescence (SIF) for Regional Drought Monitoring, *Agriculture*, 12, 547, <https://doi.org/10.3390/agriculture12040547>, 2022.

Hu, J., Liu, L., Guo, J., Du, S., and Liu, X.: Upscaling Solar-Induced Chlorophyll Fluorescence from an Instantaneous to Daily Scale Gives an Improved Estimation of the Gross Primary Productivity, *Remote Sensing*, 10, 1663, 2018.

Hussain, M. and Mahmud, I.: pyMannKendall: a python package for non parametric Mann Kendall family of trend tests, *Journal of open source software*, 4, 1556, <https://doi.org/10.21105/joss.01556>, 2019.

Jeong, S., Ryu, Y., Gentine, P., Lian, X., Fang, J., Li, X., Dechant, B., Kong, J., Choi, W., Jiang, C., Keenan, T. F., Harrison, S. P., and Prentice, I. C.: Persistent global greening over the last four decades using novel long-term vegetation index data with enhanced temporal consistency, *Remote Sensing of Environment*, 311, 114282, <https://doi.org/10.1016/j.rse.2024.114282>, 2024.

Joiner, J., Yoshida, Y., Vasilkov, A. P., Yoshida, Y., Corp, L. A., and Middleton, E. M.: First observations of global and seasonal terrestrial chlorophyll fluorescence from space, *Biogeosciences*, 8, 637–651, <https://doi.org/10.5194/bg-8-637-2011>, 2011.

Joiner, J., Guanter, L., Lindstrom, R., Voigt, M., Vasilkov, A. P., Middleton, E. M., Huemmrich, K. F., Yoshida, Y., and Frankenberg, C.: Global monitoring of terrestrial chlorophyll fluorescence from moderate-spectral-resolution near-infrared satellite measurements: methodology, simulations, and application to GOME-2, *Atmos. Meas. Tech.*, 6, 2803–2823, <https://doi.org/10.5194/amt-6-2803-2013>, 2013.

Joiner, J., Yoshida, Y., Koehler, P., Frankenberg, C., and Parazoo, N. C.: L2 Daily Solar-Induced Fluorescence (SIF) from ERS-2 GOME, 1995–2003, ORNL DAAC [data set], <https://doi.org/10.3334/ORNLDAA/1758>, 2019.

Joiner, J., Yoshida, Y., Koehler, P., Frankenberg, C., and Parazoo, N. C.: L2 Solar-Induced Fluorescence (SIF) from SCIAMACHY, 2003–2012, ORNL DAAC [data set], <https://doi.org/10.3334/ORNLDAA/1871>, 2021.

Ju, W. and Zhou, Y.: Global Daily GPP Simulation Dataset from 1981 to 2019, National Ecosystem Science Data Center [data set], <https://doi.org/10.12199/nesdc.ecodb.2016YFA0600200.02.001>, 2021.

Khakurel, P., Leigh, L., Kaewmanee, M., and Pinto, C. T.: Extended pseudo invariant calibration site-based trend-to-trend cross-calibration of optical satellite sensors, *Remote Sensing*, 13, 1545, <https://doi.org/10.3390/rs13081545>, 2021.

Köhler, P., Guanter, L., and Joiner, J.: A linear method for the retrieval of sun-induced chlorophyll fluorescence from GOME-2 and SCIAMACHY data, *Atmos. Meas. Tech.*, 8, 2589–2608, <https://doi.org/10.5194/amt-8-2589-2015>, 2015.

Koren, G., van Schaik, E., Araújo, A. C., Boersma, K. F., Gärtner, A., Killaars, L., Kooreman, M. L., Kruijt, B., van der Laan-Luijkx, I. T., von Randow, C., Smith, N. E., and Peters, W.: Widespread reduction in sun-induced fluorescence from the Amazon during the 2015/2016 El Niño, *Philosophical Transactions of the Royal Society B: Biological Sciences*, 373, 20170408, <https://doi.org/10.1098/rstb.2017.0408>, 2018.

Li, X. and Xiao, J.: A Global, 0.05-Degree Product of Solar-Induced Chlorophyll Fluorescence Derived from OCO-2, MODIS, and Reanalysis Data, *Remote Sensing*, 11, 517, <https://doi.org/10.3390/rs11050517>, 2019.

Li, X., Xiao, J., and He, B.: Chlorophyll fluorescence observed by OCO-2 is strongly related to gross primary productivity estimated from flux towers in temperate forests, *Remote Sensing of Environment*, 204, 659–671, <https://doi.org/10.1016/j.rse.2017.09.034>, 2018.

Lu, X., Cai, G., Zhang, X., Yu, H., Zhang, Q., Wang, X., Zhou, Y., and Su, Y.: Research on downscaling method of the enhanced TROPOMI solar-induced chlorophyll fluorescence data, *Geocarto International*, 39, 2354417, <https://doi.org/10.1080/10106049.2024.2354417>, 2024.

Ma, Y., Liu, L., Liu, X., and Chen, J.: An improved downscaled sun-induced chlorophyll fluorescence (DSIF) product of GOME-2 dataset, *European journal of remote sensing*, 55, 168–180, <https://doi.org/10.1080/22797254.2022.2028579>, 2022.

Markham, B. L. and Helder, D. L.: Forty-year calibrated record of earth-reflected radiance from Landsat: A review, *Remote Sensing of Environment*, 122, 30–40, <https://doi.org/10.1016/j.rse.2011.06.026>, 2012.

Mishra, N., Haque, M. O., Leigh, L., Aaron, D., Helder, D., and Markham, B.: Radiometric Cross Calibration of Landsat 8 Operational Land Imager (OLI) and Landsat 7 Enhanced Thematic Mapper Plus (ETM+), *Remote Sensing*, 6, 12619–12638, 2014.

Mohammed, G. H., Colombo, R., Middleton, E. M., Rascher, U., van der Tol, C., Nedbal, L., Goulas, Y., Pérez-Priego, O., Damm, A., Meroni, M., Joiner, J., Cogliati, S., Verhoef, W., Malenovský, Z., Gastellu-Etchegorry, J.-P., Miller, J. R., Guanter, L., Moreno, J., Moya, I., Berry, J. A., Frankenberg, C., and Zarco-Tejada, P. J.: Remote sensing of solar-induced chlorophyll fluorescence (SIF) in vegetation: 50 years of progress, *Remote Sensing of Environment*, 231, 111–177, <https://doi.org/10.1016/j.rse.2019.04.030>, 2019.

OCO-2/OCO-3 Science Team, Payne, V., and Chatterjee, A.: OCO-2 Level 2 bias-corrected solar-induced fluorescence and other select fields from the IMAP-DOAS algorithm aggregated as daily files, Goddard Earth Sciences Data and Information Services Center (GES DISC) [data set], <https://doi.org/10.5067/OTRE7KQS8AU8>, 2020.

Parazoo, N. C., Frankenberg, C., Köhler, P., Joiner, J., Yoshida, Y., Magney, T., Sun, Y., and Yadav, V.: Towards a Harmonized Long-term Spaceborne Record of Far-red Solar-induced Fluorescence, *Journal of Geophysical Research: Biogeosciences*, 124, <https://doi.org/10.1029/2019JG005289>, 2019.

Pastorello, G., Trotta, C., Canfora, E., et al.: The FLUXNET2015 dataset and the ONEFlux processing pipeline for eddy covariance

data, *Scientific Data*, 7, 225, <https://doi.org/10.1038/s41597-020-0534-3>, 2020.

Porcar-Castell, A., Tyystjärvi, E., Atherton, J., Tol, C., Flexas, J., Pfundel, E., Moreno, J., Frankenberg, C., and Berry, J.: Linking chlorophyll a fluorescence to photosynthesis for remote sensing applications: Mechanisms and challenges, *Journal of experimental botany*, 65, <https://doi.org/10.1093/jxb/eru191>, 2014.

Rascher, U., Alonso, L., Burkart, A., Cilia, C., Cogliati, S., Colombo, R., Damm, A., Drusch, M., Guanter, L., Hanus, J., Hyvärinen, T., Julitta, T., Jussila, J., Kataja, K., Kokkalis, P., Kraft, S., Kraska, T., Matveeva, M., Moreno, J., Muller, O., Panigada, C., Pilkl, M., Pinto, F., Prey, L., Pude, R., Rossini, M., Schickling, A., Schurr, U., Schüttemeyer, D., Verrelst, J., and Zemek, F.: Sun-induced fluorescence – a new probe of photosynthesis: First maps from the imaging spectrometer HyPlant, *Global Change Biology*, 21, 4673–4684, <https://doi.org/10.1111/gcb.13017>, 2015.

Ryu, Y., Jiang, C., Kobayashi, H., and Dettò, M.: MODIS-derived global land products of shortwave radiation and diffuse and total photosynthetically active radiation at 5 km resolution from 2000, *Remote Sensing of Environment*, 204, 812–825, 2018.

Ryu, Y., Berry, J. A., and Baldocchi, D. D.: What is global photosynthesis? History, uncertainties and opportunities, *Remote Sensing of Environment*, 223, 95–114, <https://doi.org/10.1016/j.rse.2019.01.016>, 2019.

Schaaf, C. and Wang, Z.: MODIS/Terra+Aqua BRDF/Albedo Nadir BRDF-Adjusted Ref Daily L3 Global 0.05Deg CMG V061, NASA Land Processes Distributed Active Archive Center [data set], <https://doi.org/10.5067/MODIS/MCD43C4.061>, 2021.

Shekhar, A., Chen, J., Bhattacharjee, S., Buras, A., Castro, A. O., Zang, C. S., and Rammig, A.: Capturing the Impact of the 2018 European Drought and Heat across Different Vegetation Types Using OCO-2 Solar-Induced Fluorescence, *Remote Sensing*, 12, <https://doi.org/10.3390/rs12193249>, 2020.

Sun, Y., Fu, R., Dickinson, R., Joiner, J., Frankenberg, C., Gu, L., Xia, Y., and Fernando, N.: Drought onset mechanisms revealed by satellite solar-induced chlorophyll fluorescence: Insights from two contrasting extreme events, *Journal of Geophysical Research: Biogeosciences*, 120, 2427–2440, <https://doi.org/10.1002/2015JG003150>, 2015.

Sun, Y., Frankenberg, C., Wood, J. D., Schimel, D. S., Jung, M., Guanter, L., Drewry, D. T., Verma, M., Porcar-Castell, A., Griffis, T. J., Gu, L., Magney, T. S., Köhler, P., Evans, B., and Yuen, K.: OCO-2 advances photosynthesis observation from space via solar-induced chlorophyll fluorescence, *Science*, 358, eaam5747, <https://doi.org/10.1126/science.aam5747>, 2017.

Tao, S., Chen, J. M., Zhang, Z., Zhang, Y., Ju, W., Zhu, T., Wu, L., Wu, Y., and Kang, X.: A high-resolution satellite-based solar-induced chlorophyll fluorescence dataset for China from 2000 to 2022, *Scientific Data*, 11, 1286, [10.1038/s41597-024-04101-6](https://doi.org/10.1038/s41597-024-04101-6), 2024.

Tavora, J., Jiang, B., Kiffney, T., Bourdin, G., Gray, P. C., de Carvalho, L. S., Hesketh, G., Schild, K. M., Faria de Sousa, L., Brady, D. C., and Boss, E.: Recipes for the Derivation of Water Quality Parameters Using the High-Spatial-Resolution Data from Sensors on Board Sentinel-2A, Sentinel-2B, Landsat-5, Landsat-7, Landsat-8, and Landsat-9 Satellites, *Journal of Remote Sensing*, 3, 0049, <https://doi.org/10.34133/remotesensing.0049>, 2023.

van Schaik, E., Kooreman, M. L., Stammes, P., Tilstra, L. G., Tuinder, O. N. E., Sanders, A. F. J., Verstraeten, W. W., Lang, R., Cacciari, A., Joiner, J., Peters, W., and Boersma, K. F.: Improved SIFTER v2 algorithm for long-term GOME-2A satellite retrievals of fluorescence with a correction for instrument degradation, *Atmos. Meas. Tech.*, 13, 4295–4315, <https://doi.org/10.5194/amt-13-4295-2020>, 2020.

Verma, M., Friedl, M. A., Law, B. E., Bonal, D., Kiely, G., Black, T. A., Wohlfahrt, G., Moors, E. J., Montagnani, L., Marcolla, B., Toscano, P., Varlagin, A., Roupsard, O., Cescatti, A., Arain, M. A., and D'Odorico, P.: Improving the performance of remote sensing models for capturing intra- and inter-annual variations in daily GPP: An analysis using global FLUXNET tower data, *Agricultural and Forest Meteorology*, 214–215, 416–429, <https://doi.org/10.1016/j.agrformet.2015.09.005>, 2015.

Verma, M., Schimel, D., Evans, B., Frankenberg, C., Beringer, J., Drewry, D. T., Magney, T., Marang, I., Hutley, L., Moore, C., and Eldering, A.: Effect of environmental conditions on the relationship between solar-induced fluorescence and gross primary productivity at an OzFlux grassland site, *Journal of Geophysical Research: Biogeosciences*, 122, 716–733, <https://doi.org/10.1002/2016JG003580>, 2017.

Wang, S., Zhang, Y., Ju, W., Wu, M., Liu, L., He, W., and Peñuelas, J.: Temporally corrected long-term satellite solar-induced fluorescence leads to improved estimation of global trends in vegetation photosynthesis during 1995–2018, *ISPRS Journal of Photogrammetry and Remote Sensing*, 194, 222–234, <https://doi.org/10.1016/j.isprsjprs.2022.10.018>, 2022.

Wen, J., Köhler, P., Duveiller, G., Parazoo, N. C., Magney, T. S., Hooker, G., Yu, L., Chang, C. Y., and Sun, Y.: A framework for harmonizing multiple satellite instruments to generate a long-term global high spatial-resolution solar-induced chlorophyll fluorescence (SIF), *Remote Sensing of Environment*, 239, 111644, <https://doi.org/10.1016/j.rse.2020.111644>, 2020.

Yang, J., Tian, H., Pan, S., Chen, G., Zhang, B., and Dangal, S.: Amazon drought and forest response: Largely reduced forest photosynthesis but slightly increased canopy greenness during the extreme drought of 2015/2016, *Global Change Biology*, 24, 1919–1934, <https://doi.org/10.1111/gcb.14056>, 2018.

Yang, X., Tang, J., Mustard, J. F., Lee, J.-E., Rossini, M., Joiner, J., Munger, J. W., Kornfeld, A., and Richardson, A. D.: Solar-induced chlorophyll fluorescence that correlates with canopy photosynthesis on diurnal and seasonal scales in a temperate deciduous forest, *Geophysical Research Letters*, 42, 2977–2987, <https://doi.org/10.1002/2015GL063201>, 2015.

Yoshida, Y., Joiner, J., Tucker, C., Berry, J., Lee, J.-E., Walker, G., Reichle, R., Koster, R., Lyapustin, A., and Wang, Y.: The 2010 Russian drought impact on satellite measurements of solar-induced chlorophyll fluorescence: Insights from modeling and comparisons with parameters derived from satellite reflectances, *Remote Sensing of Environment*, 166, 163–177, <https://doi.org/10.1016/j.rse.2015.06.008>, 2015.

Zhang, Y. and Peñuelas, J.: Combining Solar-Induced Chlorophyll Fluorescence and Optical Vegetation Indices to Better Understand Plant Phenological Responses to Global Change, *Journal of Remote Sensing*, 3, 0085, <https://doi.org/10.34133/remotesensing.0085>, 2023.

Zhang, Y., Guanter, L., Berry, J. A., van der Tol, C., Yang, X., Tang, J., and Zhang, F.: Model-based analysis of the relationship between sun-induced chlorophyll fluorescence and gross primary production for remote sensing applications, *Remote Sensing of Environment*, 187, 145–155, <https://doi.org/10.1016/j.rse.2016.10.016>, 2016.

Zhang, Y., Joiner, J., Gentine, P., and Zhou, S.: Reduced solar-induced chlorophyll fluorescence from GOME-2 during Amazon drought caused by dataset artifacts, *Global Change Biology*, 24, 2229–2230, <https://doi.org/10.1111/gcb.14134>, 2018a.

Zhang, Y., Joiner, J., Alemohammad, S. H., Zhou, S., and Gentine, P.: A global spatially contiguous solar-induced fluorescence (CSIF) dataset using neural networks, *Biogeosciences*, 15, 5779–5800, <https://doi.org/10.5194/bg-15-5779-2018>, 2018b.

Zhang, Y., Zhang, Q., Liu, L., Zhang, Y., Wang, S., Ju, W., Zhou, G., Zhou, L., Tang, J., Zhu, X., Wang, F., Huang, Y., Zhang, Z., Qiu, B., Zhang, X., Wang, S., Huang, C., Tang, X., and Zhang, J.: ChinaSpec: A Network for Long-Term Ground-Based Measurements of Solar-Induced Fluorescence in China, *Journal of Geophysical Research: Biogeosciences*, 126, e2020JG006042, <https://doi.org/10.1029/2020JG006042>, 2021.

Zhang, Z., Zhang, Y., Joiner, J., and Migliavacca, M.: Angle matters: Bidirectional effects impact the slope of relationship between gross primary productivity and sun-induced chlorophyll fluorescence from Orbiting Carbon Observatory-2 across biomes, *Global Change Biology*, 24, 5017–5020, <https://doi.org/10.1111/gcb.14427>, 2018c.

Zheng, X., Zhao, W., Zhu, Z., Wang, Z., Zheng, Y., and Li, D.: Characterization and Evaluation of Global Solar-Induced Chlorophyll Fluorescence Products: Estimation of Gross Primary Productivity and Phenology, *Journal of Remote Sensing*, 4, 0173, <https://doi.org/10.34133/remotesensing.0173>, 2024.

Zhu, W., Xie, Z., Zhao, C., Zheng, Z., Qiao, K., Peng, D., and Fu, Y. H.: Remote sensing of terrestrial gross primary productivity: a review of advances in theoretical foundation, key parameters and methods, *GIScience & Remote Sensing*, 61, 2318846, <https://doi.org/10.1080/15481603.2024.2318846>, 2024.

Zou, C., Du, S., Liu, X., and Liu, L.: TCSIF: a temporally consistent global Global Ozone Monitoring Experiment-2A (GOME-2A) solar-induced chlorophyll fluorescence dataset with the correction of sensor degradation, *Earth Syst. Sci. Data*, 16, 2789–2809, <https://doi.org/10.5194/essd-16-2789-2024>, 2024.

Zou, C., Liu, L., Du, S., and Liu, X.: LHSIF: the Long-Term Harmonized Multi-Satellite SIF dataset with a resolution of  $0.05^{\circ}$  spanning 1995 to 2024, Zenodo [data set], <https://doi.org/10.5281/zenodo.16394372>, 2025.